HIGH RESOLUTION, MILLENNIAL-SCALE PATTERNS OF BED COMPENSATION ON A SAND-RICH INTRASLOPE SUBMARINE FAN, WESTERN NIGER DELTA SLOPE

Zane R. Jobe[1,6], Zoltán Sylvester[1,5], Nick Howes[1], Carlos Pirmez[4], Andrew Parker[2], Alessandro Cantelli[3], Ru Smith[1], Matt Wolinksy[1], Ciaran O'Byrne[3], Niall Slowey[2], Brad Prather[7]

1. Shell International Exploration and Production Inc., Houston TX, 77082
2. Texas A&M University, Department of Oceanography, College Station TX, 77840
3. Shell Exploration and Production Company, Houston TX
4. Shell Italia Exploration and Production, Inc., Rome, Italy 1 00144
5. Present address: Chevron Energy Technology Company, Houston TX, 77002
6. Present address: Colorado School of Mines, Department of Geology and Geological Engineering, Golden, CO, 80401
7. CarTerra, LLC, 13607 Pinerock Lane, Houston TX

ABSTRACT

Near-seafloor core and seismic-reflection data from the western Niger Delta continental slope document the facies, architecture, and evolution of submarine channel and intraslope submarine fan deposits. The submarine channel enters an 8 km long x 8 km wide intraslope basin, where more than 100 m of deposits form an intraslope submarine fan. Lobe deposits in the intraslope submarine fan show no significant downslope trend in sand presence or grain size, indicating that flows were bypassing sediment through the basin. This unique dataset indicates that intraslope lobe deposits may have more sand-rich facies near lobe edges than predicted by traditional lobe facies models, and that thickness patterns in intraslope submarine fans do not necessarily correlate with sand presence and/or quality.

Core and radiocarbon age data indicate that sand beds progressively stack southward during the late Pleistocene, resulting in the compensation of at least two lobe elements. The youngest lobe element is well characterized by core data and is sand-rich, ~ 2 km wide x 6 km long, > 1 m thick, and was deposited rapidly over ca. 4,000 yr, from 18-14 ka. Sand beds

forming an earlier lobe element were deposited on the northern part of the fan from ca. 25 to 18 ka. Seafloor geomorphology and amplitudes from seismic reflection data confirm the location and age of these two compensating lobe elements. A third compensation event would have shifted sand deposition back to the northern part of the fan, but sediment supply was interrupted by rapid sea level rise during Meltwater Pulse 1-A at ca. 14 ka, resulting in abandonment of the depositional system.

INTRODUCTION

Sand-rich bodies accumulating in unconfined submarine depositional environments are referred to generically as 'lobes' (e.g., Deptuck et al., 2008). The progressive stacking of lobes and channels builds submarine fans (Normark, 1970), which are volumetrically the largest sediment accumulations on Earth (Covault, 2011) and host vast hydrocarbon reserves (Piper and Normark, 2001). The traditional facies model for submarine lobe deposits is based on observations from the modern seafloor (Normark, 1970), outcrops of lobe deposits (Bouma, 1962; Mutti and Ricci-Lucchi, 1972; Walker, 1978; Mutti and Normark, 1987; Smith, 1987), and flume tank experiments (Luthi, 1981; Parsons et al., 2002; Cantelli et al., 2011; Fernandez et al., 2014). These observations indicate that lobes display a downstream and axis to off-axis decrease in thickness, grain size, sand content, and sand bed amalgamation. This model has been validated with the acquisition of high-resolution seismic reflection and core data (e.g., Deptuck et al., 2008; Jegou et al., 2008).

This facies model, however, was derived from terminal lobes on basin floors with smooth bathymetric profiles. Variations to this facies model have been considered in areas where complex slope and seafloor morphology were present (Mutti and Normark, 1987; Piper and Normark, 2001; Smith, 2004). Complex slope morphology due to tectonics or mobile substrates can result in lobe deposition in areas of intraslope accommodation (Prather et al., 1998; Adeogba et al., 2005; Sylvester et al., 2015). Lobe deposition in intraslope settings has been well documented with seismic reflection data (Pirmez et al., 2000; Adeogba et al., 2005; Prelat et al., 2010; Pirmez et al., 2012; Prather et al., 2012a, 2012b; Sylvester et al., 2012), but few examples have lithologic (i.e., core) and/or age calibration. Using three-dimensional (3D) seismic data and

35 piston cores with radiocarbon ages, this study documents the facies, architecture, and millennial-scale bed compensation patterns of intraslope lobe deposits on the western Niger Delta continental slope (Fig. 1).

Terminology and hierarchy of depositional elements

Lobe deposits are hierarchical due to compensational stacking, and this study follows the hierarchy developed by Prelat et al (2010). In order of increasing dimensions and complexity, the hierarchy consists of beds/bedsets, lobe elements, lobes, and lobe complexes (Prelat et al., 2010). Beds are deposited by turbidity currents and have internal sedimentary structures (e.g., Bouma or Lowe divisions; Bouma, 1962; Lowe, 1982). Beds and bedsets stack to form lobe elements, which are generally a few meters thick and kilometers in length and width (Prelat et al., 2010). One or more lobe elements stack to form a lobe, which is fed by a single channel. Avulsion or significant migration of the channel creates a new lobe, and thus a lobe complex (Prelat et al., 2010). This terminology has typically been used to describe base-of-slope lobe deposits. Various other terms have arisen to describe intraslope lobe deposits: 'transient fan' (Adeogba et al., 2005), 'intraslope lobe' (Flint et al., 2011) and 'perched slope apron' (Prather et al., 2012a). We will use the term 'intraslope submarine fan' to avoid confusion between lobe dimensions and stacking patterns and the more general term 'fan' (Normark, 1970), with the understanding that lobe deposits that compose an intraslope submarine fan may have different morphology and facies architecture due to their intraslope setting.

DATASET AND METHODS

Approximately 100 km^2 of 3D seismic reflection data were interpreted for this study (Figs. 1, 2). The 3D survey is pre-stack time-migrated, 90 degree phase rotated (quadrature), with a bin spacing (i.e., horizontal resolution) of 12.5 m (x) x 18.75 m (y). The dominant frequency is 60 Hertz, resulting in a vertical resolution, or tuning thickness, of ~ 8.3 m. All reported thicknesses were converted from time to depth using a compressional velocity of 2,000 m/s, characteristic of shallowly buried deep-marine sediments (e.g., Flood et al., 1997). Thirty-

five piston cores were collected in the study area (Fig. 2) with an average length and recovery of 4.4 m and 72%, respectively. Figures DR1 and DR2 show detailed core descriptions, photos, x-rays, radiocarbon ages, and more than 100 grain-size samples analyzed using a Malvern Mastersizer 2000 particle size analyzer[1]. In order to attain radiocarbon ages, samples were taken from 6 cm thick muddy intervals in the cores and trimmed to avoid contamination from core edges. These samples were wet-sieved and the residue was picked to obtain ~10 mg of the near-surface dwelling planktonic foraminifera *Globigerinoides ruber*. Picked foram samples were pulse-sonicated in methanol to remove clays trapped inside the shell and then analyzed at the Center for Accelerated Mass Spectrometry at the Lawrence Livermore National Laboratory. The ages were calibrated and reservoir corrected using Calib 7.0 (Stuiver et al., 2005) and the MARINE13 calibration dataset (Reimer et al., 2009). A standard 400 yr marine reservoir age was applied to all ages, as no local refinements are available. All quoted ages are given in years before present (see Table DR1 [see footnote 1]).

NIGER DELTA

Modern Niger Delta

The Niger delta is one of the largest sediment accumulations in the world (~140,000 km^2 and 12 km thick) and is a prolific hydrocarbon province (Allen, 1964, 1965; Evamy et al., 1978; Doust and Omatsola, 1989). The Niger River has a large but semi-arid drainage area of 1.2 x 10^6 km^2, providing the delta with an annually averaged discharge of 6,140 m^3/s and sediment load of 1,270 kg/s (Mulder and Syvitski, 1995). Rapid Neogene sedimentation and associated progradation created gravity-induced tectonism that has resulted in significant intraslope accommodation (Damuth, 1994). The study area is located in ~ 1200 m water depth on the continental slope of the western Niger delta, where shale diapirs and ridges are common features that create intraslope accommodation (Fig. 1).

X channel and intraslope submarine fan

Pirmez et al. (2000) first studied the modern turbidite depositional systems in the study area, identifying the X, Y and Y' channels (Fig. 2). The X and Y' channels are tributaries to the Y channel (Fig. 2). Seafloor bathymetry and core data were used as inputs for a 3D numerical model that simulated turbidity currents for the Y channel (Abd El-Gawad et al., 2012a) and X channel (Abd El-Gawad et al., 2012b). The Y channel shows distinct temporal changes in stratigraphic architecture related to variations in sediment supply and tributary activity (Jobe et al., 2015). This study focuses on the X channel, which flows southwest for ~ 80 km from the shelf edge and crosses a complex slope profile (Fig. 2; Fig. 4 of Prather et al., 2012a). The X channel terminates at ~ 1,200 m water depth at an abrupt decrease in slope caused by shale diapirism that creates an intraslope basin (Fig. 2; Pirmez et al., 2000; Prather et al., 2012a). The intraslope submarine fan occupying this intraslope basin (hereafter the X fan) has high seafloor amplitudes and a roughly circular shape with a diameter of ~ 8 km and an area of 76 km^2 (Fig. 2C). The deposits of the X fan are more than 100 m thick, and Prather et al. (2012a) subdivide the fill of the X fan into two units (Fig. 3). A core on the muddy edge of the X fan has been the focus of a West African paleoclimate study by Parker et al. (2016). Moving downslope from the X channel terminus and onto the X fan, seismic reflection character becomes increasingly continuous (Fig. 3C). Increasing slope gradient at the distal edge of the X fan causes the formation of multiple knickpoints that coalesce into a steep, short channel segment that then joins the Y channel (Fig. 2C). The presence of this 'exit' channel and a sharp decrease in seismic amplitude indicate that flows are bypassing the X fan and eroding its distal edge (Figs. 2C, 3C).

X CHANNEL FACIES AND ARCHITECTURE

The X channel has an average width of ~ 360 m (calculated from cross sections taken every 500 m along the channel reach), low sinuosity (1.25), and dominant meander half wavelengths of 1-2 km, although a few tight bends are evident (Fig. 2). Piston cores were taken in the X channel about 20 km upstream of its terminus (Figs. 2B and 4; Fig. DR1 [see footnote 1]). High seafloor seismic amplitudes suggest sand deposition in the thalweg and near-channel overbank areas (Fig. 2B). Piston cores recovered sand, gravel (up to 5 mm in diameter), and chaotic muddy units in the thalweg of the X channel and interbedded sand and mud deposits in the overbank areas (Fig. 5). Sand deposition occurred from at least 19 ka until ca. 14 ka, and an

overlying Holocene muddy drape characterizes the upper 3-4 m of every core (Figs. 4, 5). The X channel was probably active before 19 ka, but shallow core penetration does not allow characterization and dating of older channel-related deposits (Fig. 5B). Sand beds are thicker (average 5.4 cm) in the X channel thalweg than in overbank areas (average 3.1 cm; Fig. 4). Visual core descriptions indicate that the thicker thalweg sand beds are also coarser grained, with one bed having granules 5 mm in diameter (inset photo in Fig. 4B). Grain size analyses from a laser particle size analyzer (histograms in Fig. 4) confirm this trend, with average $D_{10}/D_{50}/D_{90}$ values in the thalweg cores of 62/175/315 μm vs. 77/129/216 μm in the overbank cores. Thick T_{abc} sand beds show normal grading and an improvement in sorting from base to top (Fig. 4), suggesting deposition from turbidity currents (Bouma, 1962; Lowe, 1982). A muddy, ~ 1m thick muddy unit with sheared fabric and discontinuous silty laminae (Fig. 4B, core Bend 4) suggests deposition by mass failure. A radiocarbon age in this mass transport deposit (MTD; Fig. 4B) is older than 50 ka, suggesting this unit was derived from older sediments, perhaps a nearby bank collapse or updip slope failure.

The overbank areas on the outer and inner bends of the X channel have very different architecture (Fig. 5). The levee on the outer bank thins and dims away from the X channel on seismic data (Fig. 5B), and cores show sand-bed thinning (e.g., cores Bend 2 to Bend 7, Fig. 5A), consistent with observations of other external levees (Hansen et al., 2015). The deposition rate for the distal part of the outer levee is 67 cm/k.y. (core Bend 5, Fig. 4A); proximal levee deposition rates are likely much higher (e.g., core Bend 2), but poor core recovery prevented sampling. The overbank area on the inner bend of the X channel (Fig. 5B) does not display levee morphology, but rather is a low elevation terrace, likely caused by lateral migration of the X channel (Fig. 5A, B; cf. Babonneau et al., 2010; Maier et al., 2012; Hansen et al., 2015). Low seismic resolution prevents detailed imaging of the internal architecture of the terrace, but core data (core Bend 6 in Fig. 5A) indicate a sand-rich environment. The lower elevation of the inner-bend terrace as compared to the outer-bend levee allowed for more than 2 m of amalgamated sand beds to be deposited (core Bend 6 in Figs. 4C, 5A). Radiocarbon age correlations indicate that sand deposition on the inner levee terrace was concurrent with outer levee sand deposition and emplacement of intra-thalweg sand, gravel, and MTDs (Fig. 5A).

INTRASLOPE SUBMARINE FAN ARCHITECTURE

Seafloor morphology

The X channel terminates into an intraslope basin that contains a 8 km x 8 km x 120 m thick sediment body termed the X intraslope submarine fan (X fan; Fig. 2C). Bathymetric cross sections spaced every 500 m (Fig. 6) and three seismic cross sections (Fig. 3D) show mounding of the proximal area of the X fan (near the channel mouth), while the distal area is relatively flat. The proximal mounding is roughly symmetrical and emanates from the X channel terminus (Figs. 6, 7A). Slope gradients on the X fan are low (Fig. 7A; average gradient 1.4º, 82% of values are < 2º). The mouth of the X channel has sediment waves (Fig. 17 of Prather et al., 2012a) and the northern levee continues onto the X fan as a ridge that curves and tapers to the south (Fig. 7A). Slope gradient (i.e., dip magnitude) and aspect (i.e., dip azimuth) maps (Fig. 7) clearly delineate this ridge and show the continuity from the X channel to the southern part of the X fan. Immediately downstream of the termination of the ridge there are two large (up to 1000 m long) scours, the larger of which is cored (core Fan 11, Figs. 7A and 8). This seafloor morphology suggests that the most recent flows exiting the X channel were directed onto the southern portion of the X fan, and the aspect map (Fig. 7B) reveals a 2 km x 6 km lobate feature emanating from the X channel. In contrast, the northern part of the X fan is underfilled (left side of Fig. 6) and consequently has lower seafloor amplitudes (Fig. 2C). The presence of sediment waves suggests deposition from alternating segments of supercritical and subcritical flow, with hydraulic jumps in between (cf. Covault et al., 2014.). The sediment waves are developed close to the channel mouth where the supercritical channelized flow becomes subcritical due to the sudden decrease in slope gradient and loss of confinement. At the distal edge of the X fan, multiple knickpoints coalesce into an exit channel (Fig. 7A) that eventually joins the Y channel (Fig. 2C). The presence of this exit channel indicates that flows entering the X fan from the X channel were bypassing at least some volume of sediment. The presence of large seafloor scours (Fig. 7A) supports the interpretation of bypassing flows (Kane et al., 2009).

Sand distribution and characterization from core and seismic data

Core data indicate that areas with high seafloor amplitudes are sandy (e.g., X channel and fan) while areas with low amplitudes are predominantly muddy. To compare core data from the study area, we use the net-to-gross ratio (hereafter N:G), calculated from each core as the summed thickness of sand beds divided by the total 'gross' thickness of the core (Fig. DR2 [see footnote 1]). We exclude the hemipelagic mud-drape in each core from the N:G calculation in order to more accurately delineate lithology when the system was active. There is no significant proximal to distal trend in N:G (see bubble plot in Fig. 7A). However, a lateral increase in N:G is evident from north to south (Fig. 7A). Nine cores, mostly from the southern X fan, have N:G values larger than 0.9, while in the northern X fan, core N:G values are less than 0.5 (Fig. 7A). The southern cores also have greater mean sand bed thicknesses than the northern cores (16 vs 7 cm, bubble plot in Fig. 7B). Sand beds are normally graded and exhibit structureless bases (T_a/S_3 divisions) with parallel laminated and current ripple cross-laminated tops (T_{bc}), interpreted as the deposits of turbidity currents (Fig. 8; Bouma, 1962; Lowe, 1982). Bed amalgamation and mud clasts are common (Fig. 8A-B). Grain size analyses show a clear progression of increasing sorting and decreasing grain size from the base to the top of thick-bedded turbidites (Fig. 8D) and confirm the presence of amalgamation surfaces described in the core (Fig. 8B). Generally, sand beds deposited on the X fan are coarser-grained than in the X channel; grain size analyses demonstrate that the average $D_{10}/D_{50}/D_{90}$ on the X fan is 76/160/444 μm (n=118) while the X channel is 75/130/221 μm (n=88). The difference in the coarse fraction (e.g., D_{90}) is especially apparent when comparing grain size histograms between channel and fan (compare Figs. 4 and 8). This indicates that most of the coarser-grained fraction is likely bypassing the X channel, with only a coarse-grained bypass lag deposited in the channel thalweg (e.g., Fig. 4B). Interestingly, there is no significant trend in sand grain size across the X fan, indicating that unconfined/non-channelized flows carried even the coarsest grains in the flow for 8 km to the distal edge of the intraslope basin (Fig. 7). Supporting this inference are high amplitudes in the exit channel downdip of the X fan (Fig. 2C) and thick-bedded, coarse-grained sand beds in the most distal X fan core (core Fan 7, Fig. 7).

STACKING PATTERNS

Turbidite bed stacking at the millennial scale

The 28 piston cores provide excellent lithologic calibration for lobe deposits in the X fan (Fig. DR2 [see footnote 1]). Because cores average 4.3 m in length, the 3D seismic data could not be used for correlation due to its ~ 8 m vertical resolution (Fig. 3). Consequently, extensive radiocarbon dating of the piston cores provides the basis for inter-core correlation and calculation of sedimentation rates across the X fan. Given that most cores have > 1 km spacing, correlation of individual sand beds is sometimes uncertain, but bedsets (i.e., time-equivalent packages of sand beds) are easily correlated (Fig. 9). Time lines for 14, 18, and 25 ka (shown as dashed lines in Figs. 9, 10) were calculated by assuming a linear sedimentation rate between ages in each core and that the top of each core has an age of 0 ka. Strike-oriented core cross-sections in Figure 9 show a prominent younging of sand beds and bedsets from north to south. No sand was deposited on the northern X fan younger than 17 ka, while sand beds as young as 13.9 ka are present on the southern X fan (Fig. 9). In the most proximal strike section, sand beds are thicker and younger on the southern X fan (Fig. 9A). The youngest sands on the northern and southern X fan are 17.0 ka (core Fan 15) and 15.2 ka (core Fan 1), respectively, while X channel mouth sands have ages similar to the southern X fan (e.g., 13.9 ka in core Fan 16 3 inch; Fig. DR2 [see footnote 1]). Core Fan 17 consists of mud throughout this time interval (Fig. 9A), demonstrating the pinchout of sand against the southern basin margin (see also Fig. 2C, 3D). Core Fan 17 was also used to constrain longer-term deposition rates using oxygen isotope methodologies (see Parker et al., 2016). Radiocarbon ages from the medial strike section (Figs. 9B) indicate that sand deposition shifted southward at least 4 km in ca. 4 k.y., from 18.0 ka to 14.1 ka. The distal strike-oriented core cross-sections display the same southward younging trend (Figs. 9C-D), although poor core recovery (likely due to the presence of amalgamated, thick-bedded sands) prevents full characterization. The southward younging trend is also observed in dip-oriented core cross sections, where the youngest sand on the northern X fan is ~ 16.9 ka (Fig. 10A) while sand beds on the southern X fan are as young as 13.9 ka (Figs. 10C-D).

Back-stepping is also observed in deposits on the X fan, best shown in dip-oriented core cross sections (Fig. 10). The central dip-oriented core cross section most clearly shows the back-stepping, with progressively younger sand beds deposited towards the mouth of the X channel (19.6 ka to 13.9 ka; Fig. 10C). The southern dip section shows a similar back-stepping trend, with distal ages of ~16 ka and proximal ages of 13.9 ka (Fig. 10D). The shorter duration of back-

stepping on the southern X fan is further evidence that it was most recently active (Figs. 7B, 9, 10). Back-stepping has been observed in other lobe deposits on the modern seafloor (Deptuck et al., 2008; Prather et al., 2012b) and in flume tank experiments (Cantelli et al., 2011; Fernandez et al., 2014).

Larger-scale stacking patterns

While this study focuses on millennial-scale event bed/bedset stacking patterns, we briefly describe here the larger-scale stacking patterns on the X fan. Prather et al. (2012a) interpreted two main phases of deposition, and mapped lower and upper units (Fig. 3). Both units were deposited in the X intraslope basin (Fig. 3) and are relatively thick for their areal extent (e.g., 'confined lobes' of Prelat et al., 2010). The lower unit covers an area of 6 x 8 km and has a maximum thickness of 75 m (Fig. 3). The lower unit is thickest in the center of the X fan (Fig. 3A). The upper unit is areally larger (8 x 8 km) but thinner, with only ~ 40 m maximum thickness (Fig. 3B). Covault and Romans (2009) observed a similar trend of successively larger and thinner lobate deposits in the California Borderland. Assuming roughly constant sediment supply, this trend is the consequence of filling a bowl-shaped intraslope minibasin (Sylvester et al., 2015). The upper unit is thickest where the lower unit is thin (Fig. 3A-B), indicating large-scale compensational stacking of the lower and upper units of the X fan. Linear extrapolation from oxygen isotope age data (core Fan 17; see Parker et al., 2016) suggest that the age of the base of the upper unit is ca. 130 ka, roughly coincident with low sea level during Marine Isotope Stage (MIS; Lisiecki and Raymo, 2005) 6, and the base of the lower unit is ca. 630 ka, coincident with low sea level during MIS 16. These ages assume constant sedimentation rate through time and are thus speculative.

DISCUSSION

Compensation of Beds and Architectural Elements

This study interprets the character and timing of bed and bed-set compensation on a modern intraslope submarine fan. While other studies have described bed and bed-set compensation in modern submarine lobe deposits (e.g., Vittori et al., 2000; Deptuck et al., 2008; Jegou et al., 2008; Romans et al., 2009), this study is the first to document higher-resolution, bed-scale compensation in an intraslope basin setting. Our interpretations rely on shallow core penetrations, and while the patterns of compensation are convincing, they are not unequivocal. Additional data from deeper stratigraphy are needed to support our interpretations of bed-scale compensation during the late Quaternary. Our correlations indicate a 4 km southward shift in sand deposition that occurred over a ca. 4 k.y. period. This scale of compensation most likely represents the emplacement of two 'lobe elements' (terminology of Prelat et al., 2010) on the northern and southern parts of the X fan. The older lobe element was deposited on the northern part of the X fan from ~ 25-18 ka (Fig. 9). The most recent lobe element on the southern part of the X fan is approximately 2 km wide and 6 km long and can be seen on core cross sections (Fig. 9) and the seafloor aspect map (Fig. 7B). The thickness of the most recent lobe element is at least 1 m but is limited by core penetration; scaling from Prelat et al. (2010) suggests a thickness of 3-10 m. The seafloor geomorphology (Fig. 6) and backstepping of beds in the most recent lobe element (Fig. 10) suggests that if sand deposition had not been interrupted at 14 ka, a third lobe element would have been deposited on the northern X fan (cf. Cantelli et al., 2011). These lobe elements stack in a compensational manner to form a larger depositional element termed a lobe (cf. Prelat et al., 2010).

The larger-scale stacking patterns in the X intraslope basin seem to be compensational as well (Fig. 3; Prather et al., 2012a). The upper unit is 35 m thick and has a clearly depositional lobate shape (Fig. 3B; Fig. 15B of Prather et al., 2012a), suggesting it can be considered a 'lobe' in the scaling and hierarchy of Prelat et al. (2010). In contrast, the lower unit can be considered a lobe complex, as it is thicker (~ 75 m) and its thickness pattern is not lobate, but rather mimics the shape and subsidence pattern of the basin (Fig. 3A). This, along with the convergent nature of the seismic reflections (cf. Sylvester et al., 2015), suggests that the morphology of the lower unit is recording subsidence history rather than depositional morphology. The striking difference between the thickness patterns of the lower (lobe complex) and upper (lobe) units (Fig. 3) demonstrates the concept of the 'stratigraphic integral scale' (Sheets et al., 2002; Lyons, 2004;

Straub et al., 2009), where individual depositional elements have a process-based thickness pattern (e.g., lobe element in Fig 7B, lobe in Fig. 3B), but over longer time scales, the thickness pattern reflects the basin subsidence history (e.g. lobe complex in Fig. 3A). The duration of the lower (ca. 500 k.y.) and upper (ca. 130 k.y.) units reinforces the interpretation of the thickness patterns and hierarchical assignments.

Timing of Sand Delivery to the X Channel and Fan

Core data indicate that sand was delivered from the X channel to the X fan from at least 25 ka until 14 ka (Fig. 9). The lack of deeper cores limits knowledge of earlier deposits of the X fan, but we infer that sand was being delivered to the X fan since at least 50 ka, when the nearby Y channel was active (Jobe et al., 2015). Average deposition rates for sandy deposits on the X fan are more than two times higher than muddy deposits (35.8 vs. 13.5 cm/k.y., respectively). The youngest sand beds present in the X channel and fan were deposited at 13.5 ka and 13.9 ka, respectively (Figs. 5C, 9A). The 400 yr difference suggests that the backstepping trend observed in the youngest lobe element on the X fan (Fig. 10) may have continued up the X channel for ca. 400 yr after the end of sand deposition on the fan. This style of progressive updip abandonment has also been demonstrated in nearby submarine channel systems (Jobe et al., 2015).

The mechanism forcing the cessation of sand deposition in the study area is interpreted to be allogenic in nature, as no autogenic forcing mechanisms (e.g., submarine channel avulsions) are observed. While we cannot exclude tectonic forcing (e.g., growth fault or shale diapir movement), we have no evidence of tectonic activity at ~14 ka. Other allogenic signals, such as relative sea level and climate change, tend to be propagated very quickly from source to sink (Romans et al., 2009; Covault et al., 2010; see discussion in Romans et al., 2016). The abrupt cessation of sand delivery to the study area occurred at 14 ka, the same time period that sea level rose dramatically during Meltwater Pulse 1-A (~ 20 m in 300 yr; Deschamps et al., 2012). From 14.6 to 14.3 ka, global sea level rose from -105 m to -85 m, approximately the current water depth of the Niger shelf edge (Allen, 1964, 1965). This rapid sea level rise likely caused abrupt flooding of the continental shelf, preventing sand delivery off the shelf edge.

Facies models for lobes in intraslope settings

Traditional lobe facies models indicate a progressive decrease in sand thickness and N:G away from the lobe axis (e.g., Pyrcz et al., 2005; Deptuck et al., 2008; Prelat et al., 2009). Thickness maps similar to those in Figure 3 are often interpreted as evidence of such trends in internal properties (e.g., Pirmez et al., 2000). This study indicates, however, that the traditional facies model does not apply for lobes deposited in intraslope settings where flows are often able to bypass large volumes of mud (Fig. 11). Many turbidites on the X fan lack mudcaps and well-developed laminated T_b and T_c divisions, probably due to significant bypass of fine-grained sediment. This results in intraslope lobe deposits that are very sand-rich (Fig. 11), and thick-bedded, coarse-grained sands are present even in the most distal core location (core Fan 7 in Fig. 9D).

While this study documents the sand-rich nature of intraslope lobe deposits (Fig. 11), fine-scale heterogeneity is still present. For example, a scour imaged on Figure 7A affects bed continuity of sand beds inside (core Fan 11) and outside (core Fan 10) of the scour. These two cores are only 450 m apart, and Figure 8A-B shows the rapid facies change caused by the scour (cf. Kane et al., 2009). Although we believe that Figure 11 characterizes the differences between intraslope and base-of-slope lobes, exceptions to the sand-rich intraslope fan facies architecture are possible, and may include cases where mud-rich flows are dominant or where the intraslope basin is large compared to the flow size (e.g., Prather et al., 2012b). For natural resource prediction and production, the X channel-fan system provides a well-constrained example of sub-seismic heterogeneity that is vital in understanding inter-well connectivity in reservoirs contained in intraslope submarine fan deposits.

CONCLUSIONS

Core and seismic data on the western Niger Delta continental slope illustrate the facies architecture and temporal evolution of a linked channel-lobe depositional system in an intraslope environment. The X channel has low-sinuosity and is ~ 360 m wide, with thalweg deposits consisting of thick-bedded sand and gravel interbedded with chaotic muddy units, and overbank

deposits consisting of thin-bedded, fine-grained sands and muds. The intraslope submarine fan (X fan) at the terminus of the X channel is 8 km long x 8 km wide, and contains > 100 m of intraslope lobe deposits sourced by the X channel. There are two distinct large-scale units imaged by 3D seismic data. The lower unit is 6 x 8 km x 50 m thick and is thickest in the basin center, while the upper unit is 8 x 8 km x 25 m thick and has a pronounced southward shift in its maximum thickness. This compensation is at a large (i.e., lobe or lobe-complex) scale, and may be linked to sea level variation during the last glacial cycle (130-0 ka).

Core data indicate that deposits on the X fan are more sand-rich, thicker-bedded and coarser-grained than in the X channel, implying bypass on steeper, channelized slope gradients and deposition on lower, unconfined slope gradients. There is no significant downslope trend in grain size or net-to-gross ratio on the X fan, indicating that flows were likely bypassing some sand and most mud through the intraslope basin. This results in more sand-rich deposits and partial sediment bypass than predicted by traditional facies models for lobes, particularly near lobe/fan edges. The most recent flows exiting the X channel were directed onto the southern fan, building a lobe element ~ 2 km wide x 6 km long, and at least 1 m thick. Deposition rates average 36 cm/ky, but are locally greater than 80 cm/ky. This most recent lobe element was emplaced in only 4000 yr, from 18-14 ka. Prior to the deposition of the most recent lobe element, flows from the X channel were directed onto the northern part of the X fan, from ~ 25-18 ka. This bed-scale compensation shifted the locus of sand deposition 4 km over millennial time scales (4 ka). Radiocarbon dating, seafloor geomorphology, and 3D seismic amplitudes confirm the location and age of these two compensating lobe elements. Sand deposition in the X channel/fan was interrupted by rapid sea level rise during Meltwater Pulse 1-A at ~ 14 ka, causing abandonment of the system.

This unique dataset constrains the facies and stratigraphic architecture of bed- and lobe-scale compensation in an intraslope basin setting. Core data indicate that intraslope lobe deposits can have very different facies architecture than predicted by traditional lobe facies models, and that thickness patterns do not necessarily correlate with sand presence and net-to-gross. Further work aims to incorporate simple analytical modeling to quantify the effects of sediment flux on lobe compensation in intraslope submarine fans.

ACKNOWLEDGEMENTS

We would like to thank Shell International Exploration and Production and Shell Nigeria Exploration and Production Company for permission to publish; Fugro for collection and processing of autonomous underwater vehicle data; Mary McGann and Diablo Valley Geological Services for processing core samples, Tom Guilderson at Lawrence Livermore National Laboratory for radiocarbon dating, Texas A&M University for core storage and sampling materials, and TDI-Brooks for collection of core data. Jake Covault, Amandine Prelat, and Larissa Hansen provided insightful reviews that greatly improved the paper. Finally, this paper benefitted from discussions with Daniel Minisini, John Martin, Steve Hubbard, Brian Romans, and Neal Auchter.

Figure 1. Slope map of the seafloor on the western Niger Delta continental slope, with depth contours in black. Note the complex bathymetry produced by mobile shale, including diapirs and ridges. The white box denotes the location of Figure 2.

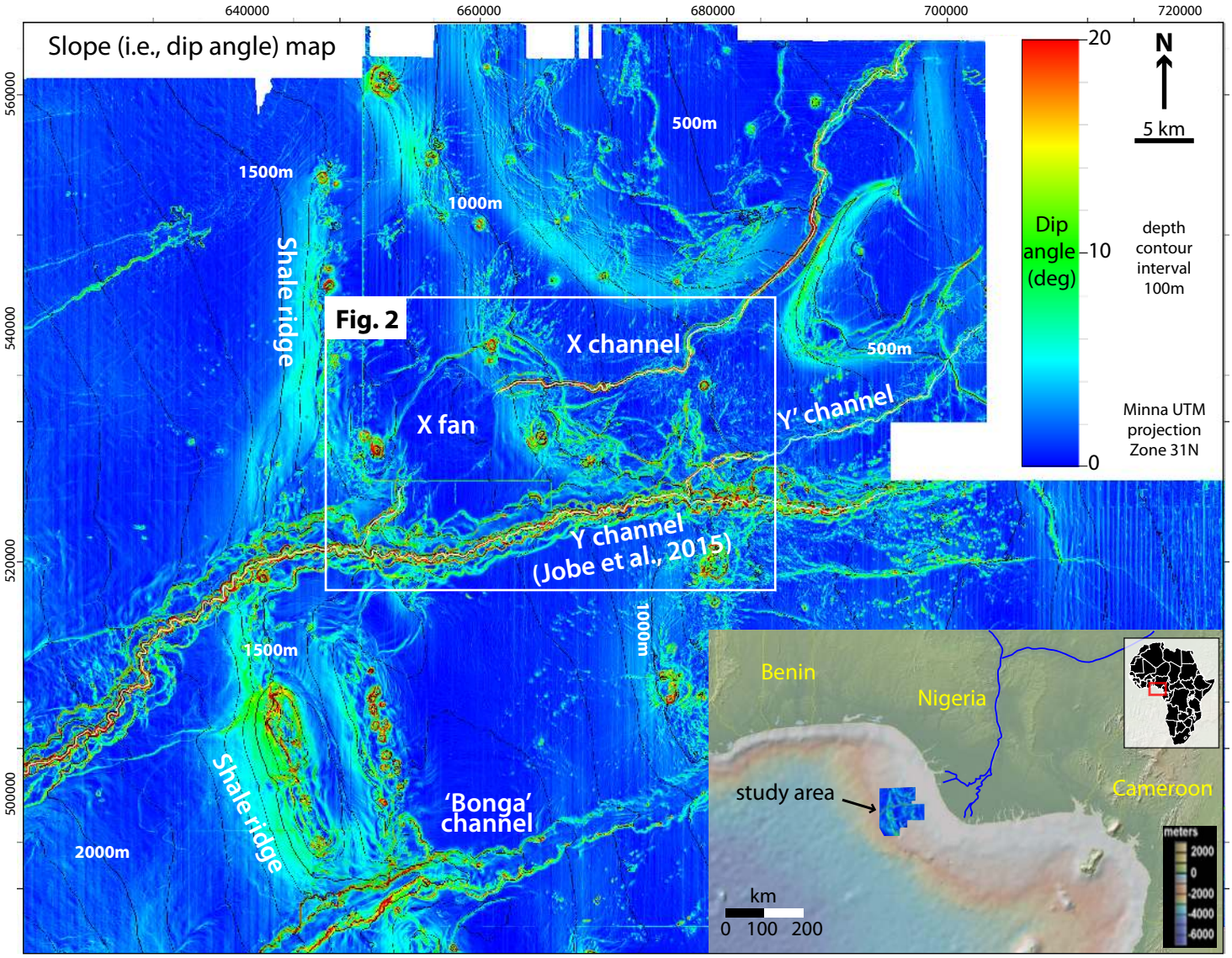
Slope (i.e., dip angle) map
640000
660000
680000
700000
720000
560000
540000
520000
500000
1500m
1000m
500m
Shale ridge
Fig. 2
X channel
X fan
Y' channel
Y channel
(Jobe et al., 2015)
1500m
1000m
Shale ridge
'Bonga'
channel
2000m
20
10
0
Dip
angle
(deg)
N
5 km
depth
contour
interval
100m
Minna UTM
projection
Zone 31N
Benin
Nigeria
Cameroon
study area
km
0 100 200
meters
2000
0
-2000
-4000
-6000

404

405 Figure 2. Bathymetric map (10 m contour interval) and seismic amplitude (color) of the seafloor.
406 (A) shows the entire study area, while (B) and (C) focus on the X channel and fan, respectively.
407 Piston core locations are shown with white circles.

408

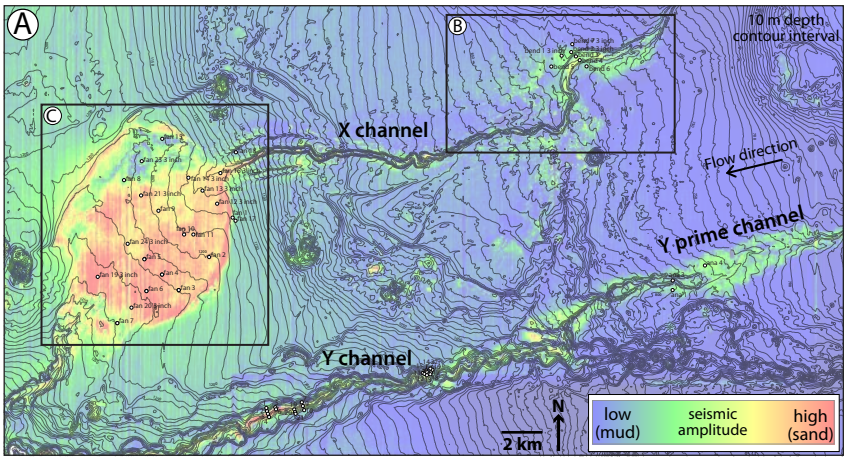
A
B
C
10 m depth contour interval
X channel
Flow direction
Y prime channel
Y channel
N
2 km
low (mud)
seismic amplitude
high (sand)

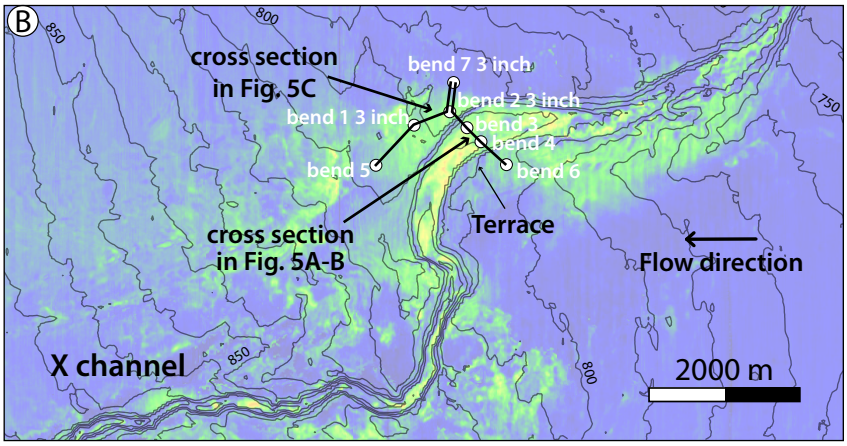
B
800
850
750
cross section in Fig. 5C
bend 7 3 inch
bend 2 3 inch
bend 1 3 inch
bend 3
bend 4
bend 5
bend 6
Terrace
cross section in Fig. 5A-B
Flow direction
X channel
2000 m

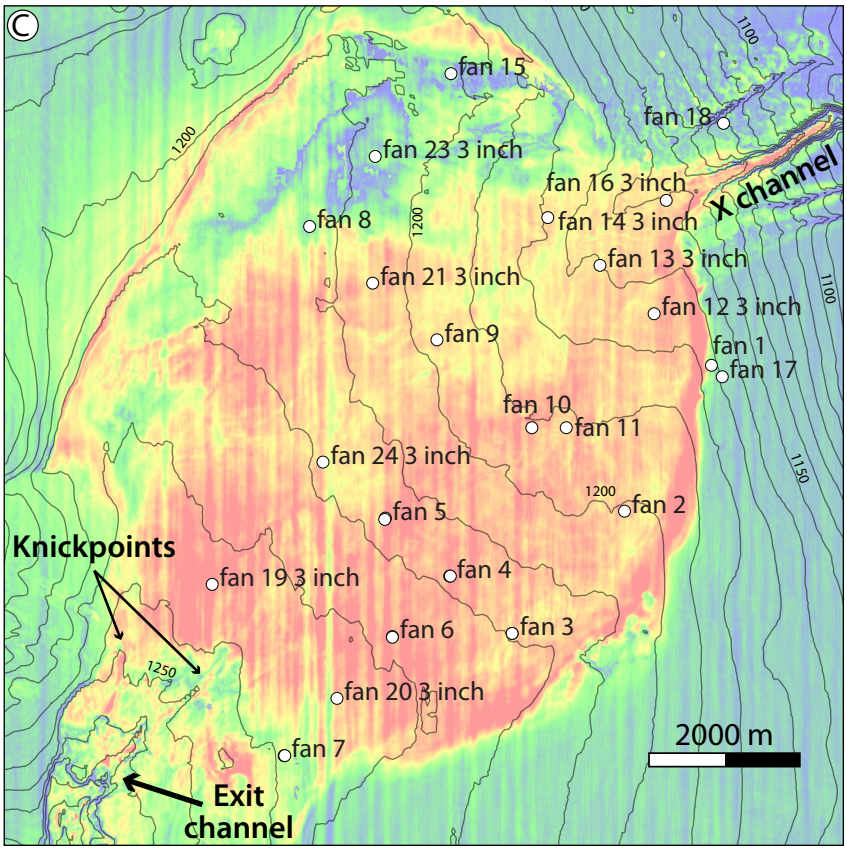
C
1100
1200
1150
1250
fan 15
fan 18
fan 23 3 inch
fan 16 3 inch
X channel
fan 8
fan 14 3 inch
fan 13 3 inch
fan 21 3 inch
fan 12 3 inch
fan 9
fan 1
fan 17
fan 10
fan 11
fan 24 3 inch
fan 5
fan 2
Knickpoints
fan 19 3 inch
fan 4
fan 6
fan 3
fan 20 3 inch
fan 7
2000 m
Exit channel

Figure 3. Characterization of the X intraslope submarine fan. (A) Thickness map of the lower unit (likely a lobe complex), with a fairly symmetric fill around the X feeder channel. (B) Thickness map of the upper unit (likely a lobe). The southward shift in thickness is caused by compensation of large-scale depositional elements (lobe to lobe-complex scale). Note the increase in areal extent in (B) as compared to (A), reflecting basin filling. (C) Dip seismic profile (red line in inset) showing the character of the intraslope basin fill and the underlying mobile shale uplifts. (D) Strike seismic profiles from the proximal, medial and distal X fan (refer to (C) for locations). Seismic character becomes more homogenous downdip and the mounded topography diminishes. Thickness maps modified after Prather et al. (2012a). VE – vertical exaggeration.

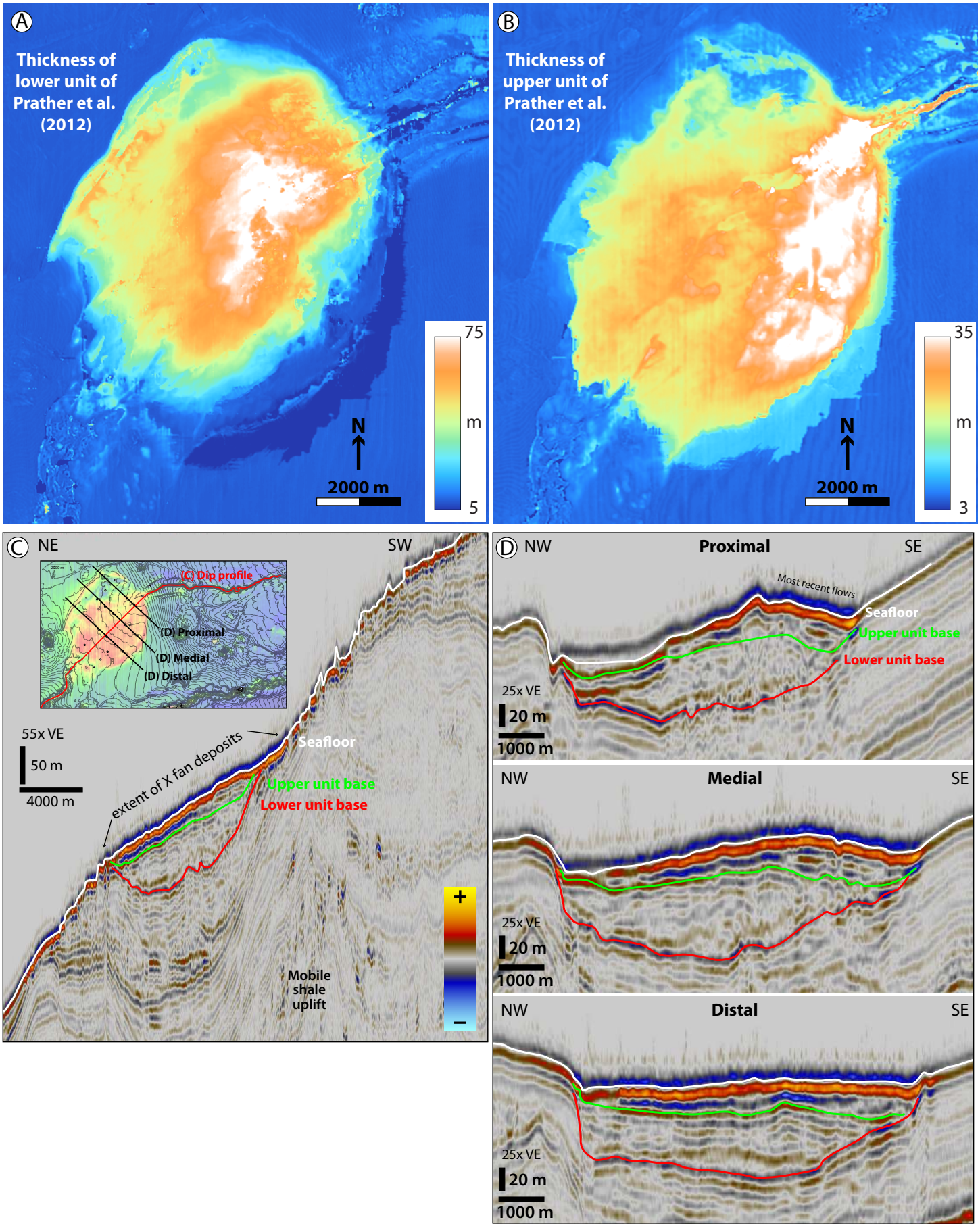
A
Thickness of lower unit of Prather et al. (2012)
75
m
5
N
2000 m
B
Thickness of upper unit of Prather et al. (2012)
35
m
3
N
2000 m
C
NE
SW
(C) Dip profile
(D) Proximal
(D) Medial
(D) Distal
55x VE
50 m
4000 m
extent of X fan deposits
Seafloor
Upper unit base
Lower unit base
Mobile shale uplift
+
–
D
NW
Proximal
SE
Most recent flows
Seafloor
Upper unit base
Lower unit base
25x VE
20 m
1000 m
NW
Medial
SE
25x VE
20 m
1000 m
NW
Distal
SE
25x VE
20 m
1000 m

Figure 4. Cores from the overbank (A, C) and thalweg (B) areas of the X channel (see Fig. 2B for core locations). Core Bend 4 was taken in the thalweg of the X channel, where coarse amalgamated sands with gravel up to 5 mm are interbedded with chaotic muddy units (interpreted as MTDs). Cores Bend 5 and Bend 6 sample overbank deposits, and have thinner bedded, finer (< 0.5 mm) ripple-laminated sands with preserved mudstone interbeds. Despite being thinly-bedded, the net-to-gross (N:G) ratio can be quite high in these overbank areas (e.g., excluding the mud drape, core Bend 5=0.44; core Bend 6=0.93).

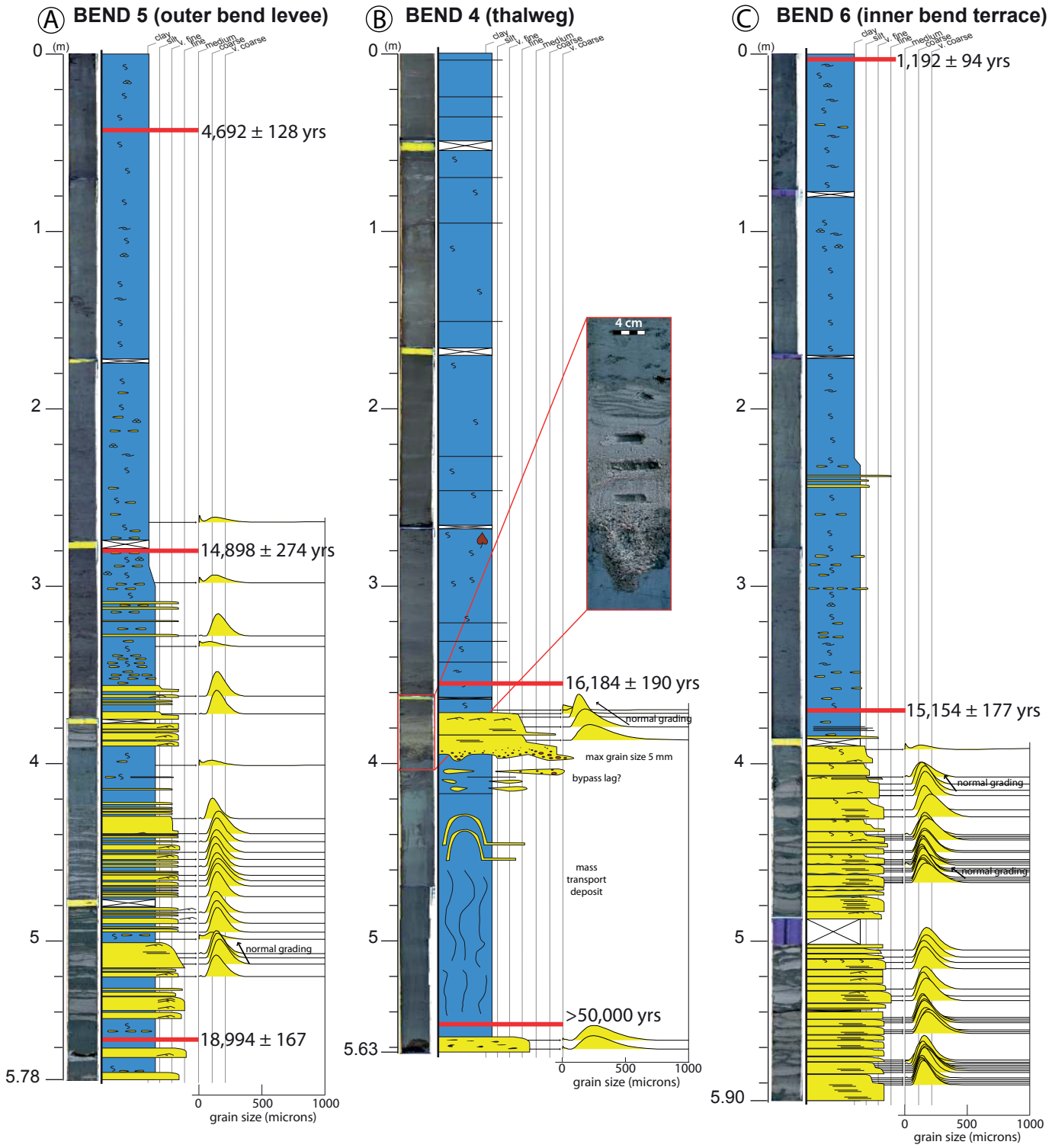
Ⓐ BEND 5 (outer bend levee)
Ⓑ BEND 4 (thalweg)
Ⓒ BEND 6 (inner bend terrace)
clay
silt
v. fine
fine
medium
coarse
v. coarse
(m)
4,692 ± 128 yrs
14,898 ± 274 yrs
18,994 ± 167
normal grading
4 cm
16,184 ± 190 yrs
max grain size 5 mm
bypass lag?
mass transport deposit
>50,000 yrs
1,192 ± 94 yrs
15,154 ± 177 yrs
grain size (microns)

Figure 5. Core cross-sections for the X channel (see Fig. 2B for location). (A) Strike-oriented section demonstrating contemporaneous sand deposition in the X channel and in both overbank areas. Note the heterogenous channel infill and the thinning of sand beds from proximal to distal overbank areas. (B) Seismic profile of (A), demonstrating the shallow core penetration (white lines) and the overbank morphology. While the outer bank has levee morphology, the inner bank has a terrace/bench morphology and thus more sand accumulation. (C) Dip-oriented core cross-section, illustrating the overbank facies architecture. Sand beds generally thin upslope and away from the X channel. MTD – mass transport deposit.

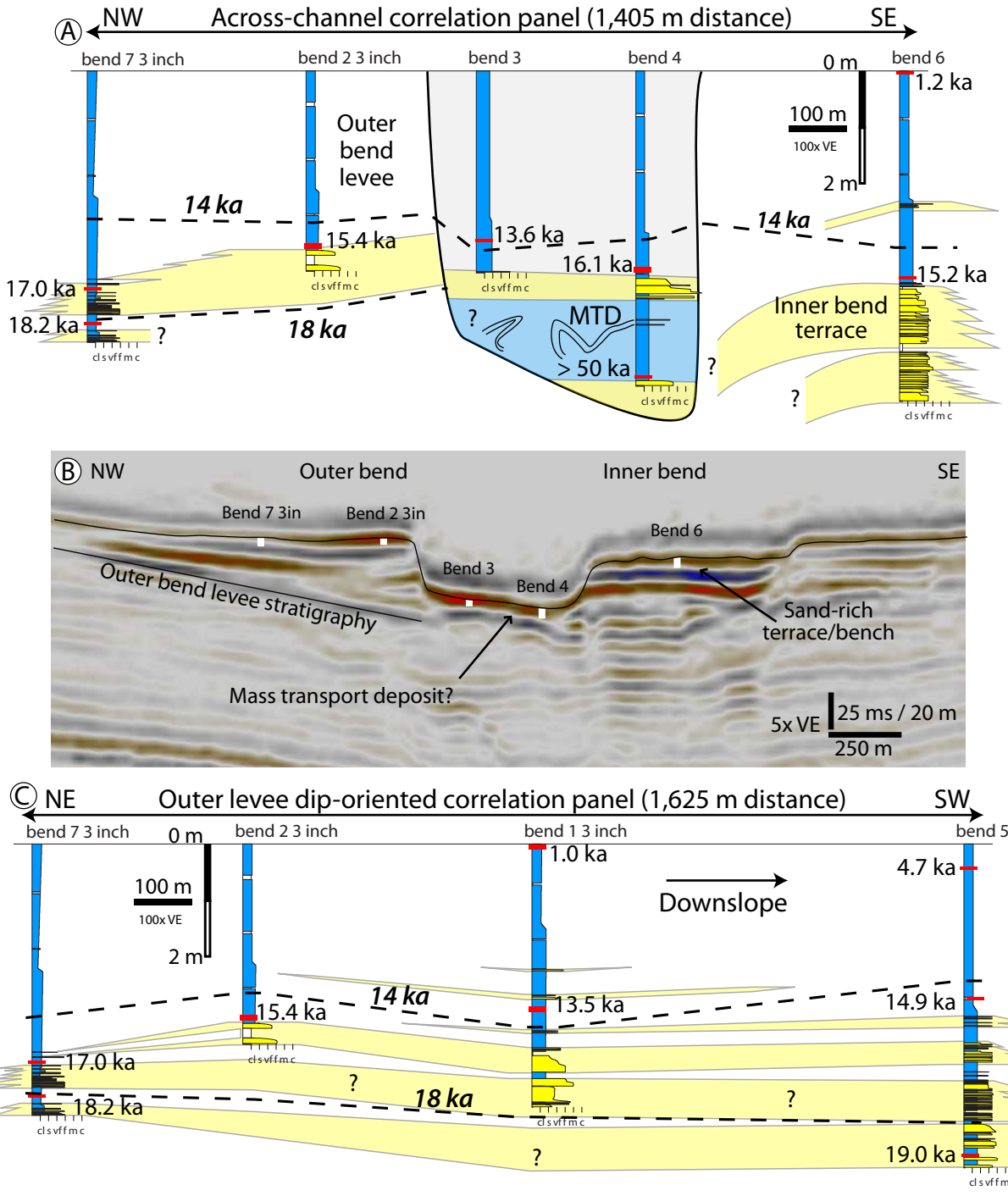
A
NW
Across-channel correlation panel (1,405 m distance)
SE
bend 7 3 inch
bend 2 3 inch
bend 3
bend 4
0 m
bend 6
1.2 ka
100 m
100x VE
2 m
Outer bend levee
14 ka
15.4 ka
13.6 ka
16.1 ka
14 ka
17.0 ka
18.2 ka
?
18 ka
MTD
> 50 ka
15.2 ka
Inner bend terrace
cl s vf f m c
B
NW
Outer bend
Inner bend
SE
Bend 7 3in
Bend 2 3in
Bend 6
Bend 3
Bend 4
Outer bend levee stratigraphy
Sand-rich terrace/bench
Mass transport deposit?
5x VE
25 ms / 20 m
250 m
C
NE
Outer levee dip-oriented correlation panel (1,625 m distance)
SW
bend 7 3 inch
0 m
bend 2 3 inch
bend 1 3 inch
bend 5
1.0 ka
4.7 ka
100 m
100x VE
Downslope
2 m
14 ka
15.4 ka
13.5 ka
14.9 ka
17.0 ka
18.2 ka
18 ka
19.0 ka

Figure 6. Bathymetric cross-sections reveal the seafloor morphology of the X fan. Note the most recent flow path is onto the southern fan due to the presence of the right-hand levee/ridge of the X feeder channel. The northern X fan is underfilled and will likely be the next area of sand deposition. Cross sections spaced every 500 m and colored from red to blue in a proximal-to-distal sense. Inset map shows cross-section locations.

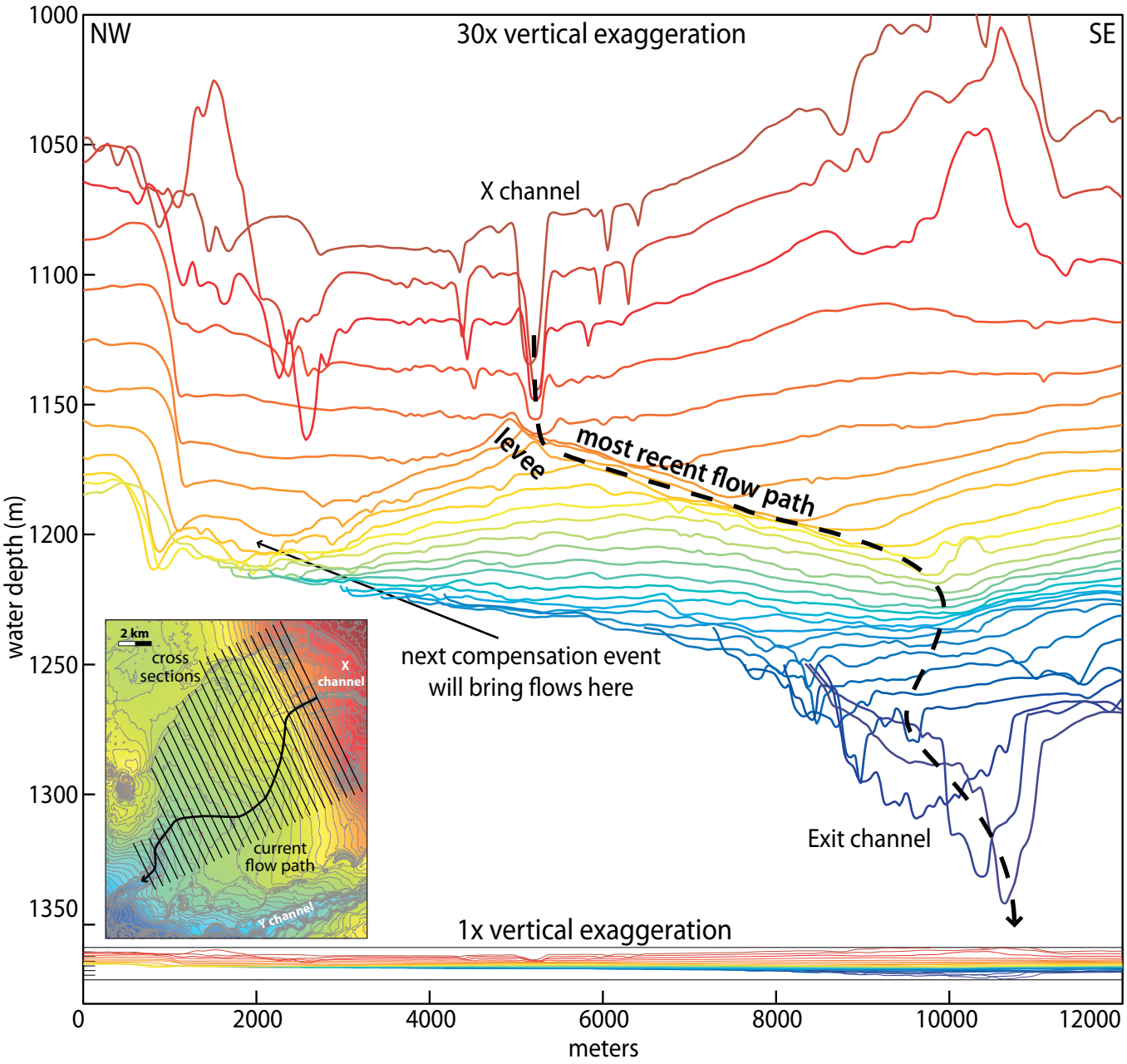
NW
30x vertical exaggeration
SE
X channel
levee
most recent flow path
next compensation event
will bring flows here
Exit channel
1x vertical exaggeration
water depth (m)
1000
1050
1100
1150
1200
1250
1300
1350
0
2000
4000
6000
8000
10000
12000
meters
2 km
cross
sections
X
channel
current
flow path
Y channel

Figure 7. Seafloor morphology of the X fan. (A) Slope (i.e., dip-angle) map with core net-to-gross (N:G) bubble plot (white circles) and individual core N:G values next to each bubble. Slope gradients on the X fan do not exceed 5 degrees, and average slope is 1.4 degrees. The right-hand levee of the X channel extends onto the fan as a ridge between cores Fan 13 and Fan 14, and two large scours are present just downslope of the ridge (Fan 11 core location). Note that the southern X fan cores have high N:G (> 0.9) while the northern X fan cores have N:G < 0.5. (B) Aspect (i.e., dip-azimuth) map with average sand thickness bubble plot (black circles). The X channel clearly feeds sediment to the southern part of the X fan, where sand beds, on average, are thicker. Dashed line shows the extent of the youngest lobe element.

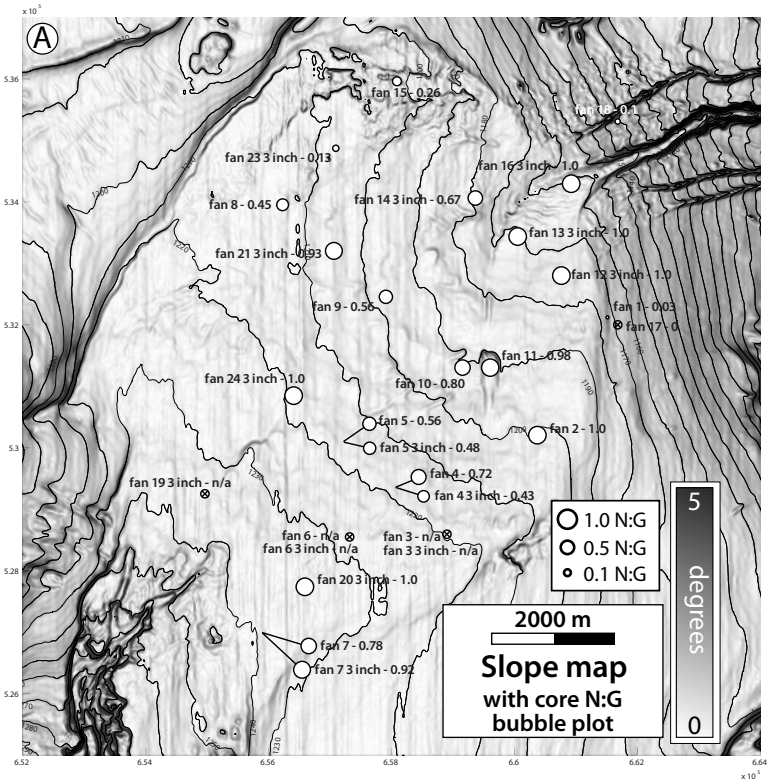
A
fan 15 - 0.26
fan 23 3 inch - 0.13
fan 16 3 inch - 1.0
fan 8 - 0.45
fan 14 3 inch - 0.67
fan 13 3 inch - 1.0
fan 21 3 inch - 0.93
fan 12 3 inch - 1.0
fan 9 - 0.56
fan 1 - 0.03
fan 17 - 0
fan 11 - 0.98
fan 24 3 inch - 1.0
fan 10 - 0.80
fan 5 - 0.56
fan 2 - 1.0
fan 5 3 inch - 0.48
fan 4 - 0.72
fan 19 3 inch - n/a
fan 4 3 inch - 0.43
fan 6 - n/a
fan 6 3 inch - n/a
fan 3 - n/a
fan 3 3 inch - n/a
fan 20 3 inch - 1.0
fan 7 - 0.78
fan 7 3 inch - 0.92
1.0 N:G
0.5 N:G
0.1 N:G
5
degrees
0
2000 m
Slope map
with core N:G
bubble plot

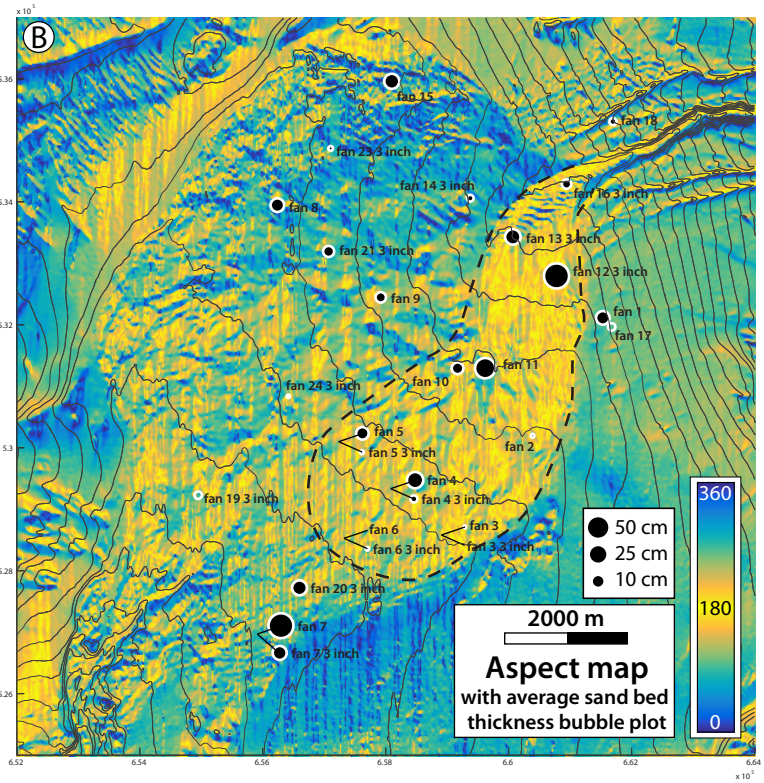
B
fan 15
fan 18
fan 23 3 inch
fan 14 3 inch
fan 16 3 inch
fan 8
fan 13 3 inch
fan 21 3 inch
fan 12 3 inch
fan 9
fan 1
fan 17
fan 11
fan 24 3 inch
fan 10
fan 5
fan 5 3 inch
fan 2
fan 4
fan 19 3 inch
fan 4 3 inch
fan 6
fan 3
fan 6 3 inch
fan 3 3 inch
fan 20 3 inch
fan 7
fan 7 3 inch
50 cm
25 cm
10 cm
360
180
0
2000 m
Aspect map
with average sand bed
thickness bubble plot

458

459 Figure 8. Details of cores on the X fan (see Fig. 7 for core locations). Muddy upper portions of
460 cores not shown. (A) and (B) Cores Fan 10 and 11 are 450 m apart on the central X fan. Core
461 Fan 11 was taken inside a scour (see Fig. 7A), and core Fan 10 just outside the scour. These
462 cores demonstrate significant lateral heterogeneity in the youngest lobe element. (C) Core Fan 15
463 on the NW part of the X fan has lower N:G, with medium-bedded sands and thick mud interbeds.
464 (D) Single sedimentation unit from core Fan 4 on the SE part of the X fan. Grain size histograms
465 show a well-defined fining and sorting upwards grain size profile. The medial/distal location of
466 core Fan 4 demonstrates that non-channelized flows were competent enough to carry very-coarse
467 sand and gravel > 5 km from the X channel mouth across a very low gradient fan surface.

468

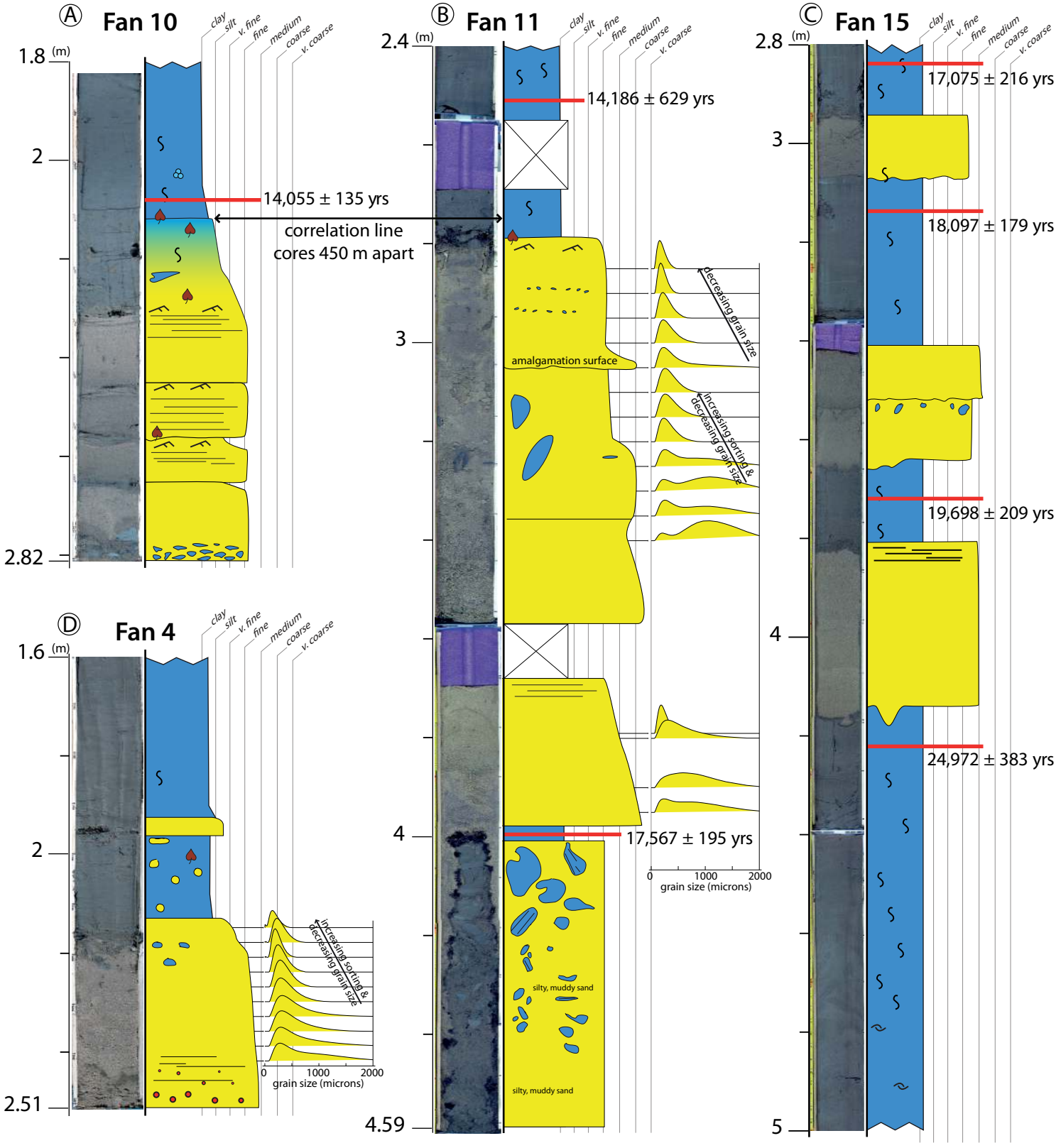
Ⓐ Fan 10
clay
silt
v. fine
fine
medium
coarse
v. coarse
1.8 (m)
2
2.82
14,055 ± 135 yrs
correlation line
cores 450 m apart
Ⓑ Fan 11
2.4 (m)
14,186 ± 629 yrs
3
amalgamation surface
decreasing grain size
increasing sorting &
decreasing grain size
4
17,567 ± 195 yrs
0
1000
2000
grain size (microns)
silty, muddy sand
silty, muddy sand
4.59
Ⓒ Fan 15
2.8 (m)
17,075 ± 216 yrs
3
18,097 ± 179 yrs
19,698 ± 209 yrs
4
24,972 ± 383 yrs
5
Ⓓ Fan 4
1.6 (m)
2
increasing sorting &
decreasing grain size
0
1000
2000
grain size (microns)
2.51

Figure 9. Strike-oriented core cross-sections on the X intraslope submarine fan. (A) Proximal strike-section, where sand beds become progressively younger from north to south, indicating 4 km of bed-scale compensation during ca. 4 k.y. (B) Medial strike-section, where progressively younger sand beds offstack to the south. (C) Medial strike-section, showing that sand beds thin and pinch out towards the NW, indicating most recent deposition on the southern X fan. (D) Distal strike-section, again showing the most recent sand deposition on the southern X fan. Note that thick-bedded sands occur at the most distal edge of the X fan, indicating that flows were able to transport sand > 5 km from the channel mouth. (E) Seafloor amplitude map with lines indicating parts A-D. The southward compensation is expressed here as hotter colors (red) indicating sand of the most recent lobe element on the southern X fan and cooler colors (blue) indicating coeval mud deposition on the northern X fan.

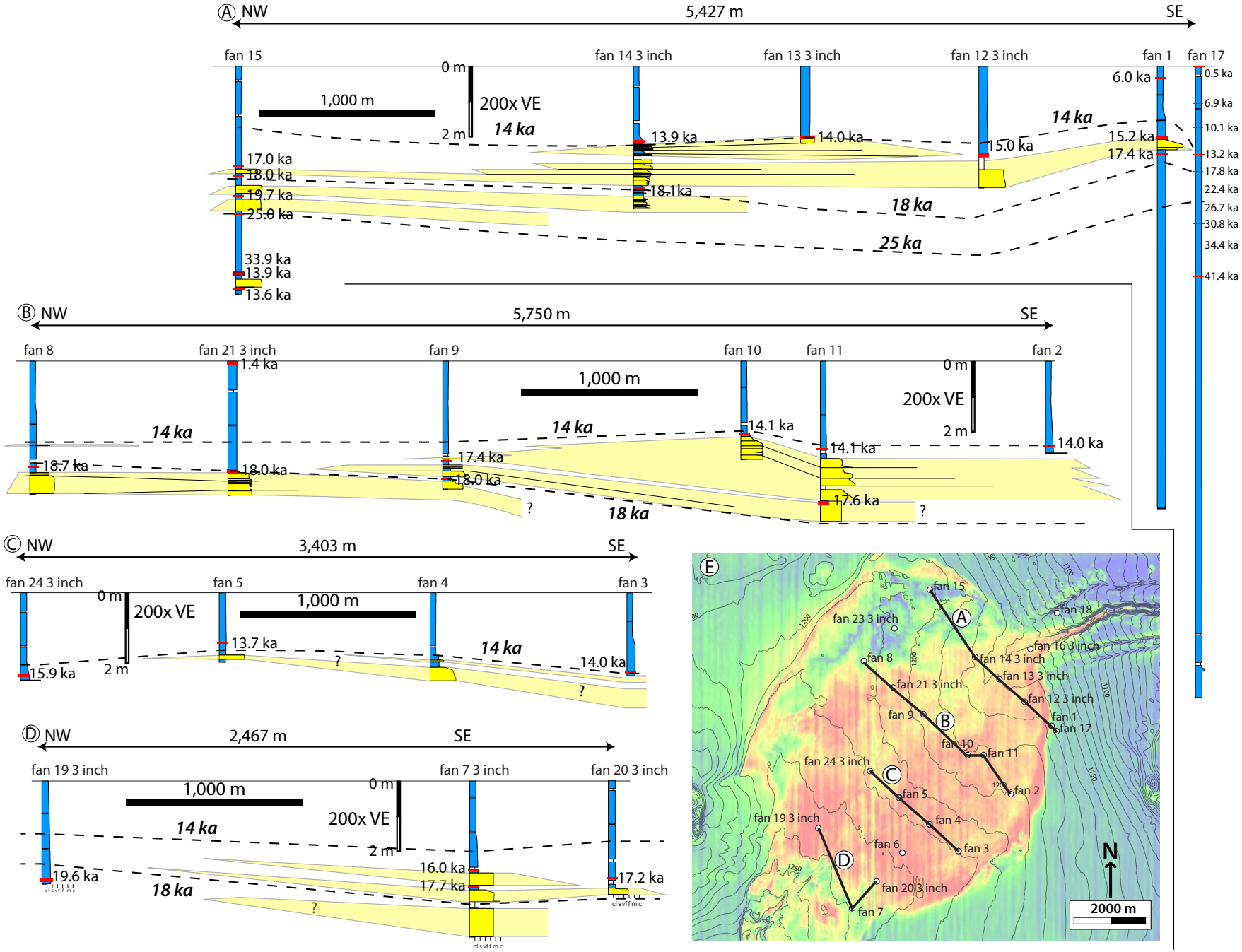
A NW
5,427 m
SE
fan 15
fan 14 3 inch
fan 13 3 inch
fan 12 3 inch
fan 1
fan 17
0 m
200x VE
2 m
1,000 m
14 ka
18 ka
25 ka
17.0 ka
18.0 ka
19.7 ka
25.0 ka
33.9 ka
13.9 ka
13.6 ka
13.9 ka
14.0 ka
15.0 ka
18.1ka
6.0 ka
15.2 ka
17.4 ka
0.5 ka
6.9 ka
10.1 ka
13.2 ka
17.8 ka
22.4 ka
26.7 ka
30.8 ka
34.4 ka
41.4 ka
B NW
5,750 m
SE
fan 8
fan 21 3 inch
fan 9
fan 10
fan 11
fan 2
1.4 ka
18.7 ka
18.0 ka
17.4 ka
18.0 ka
14.1 ka
14.1 ka
17.6 ka
14.0 ka
C NW
3,403 m
SE
fan 24 3 inch
fan 5
fan 4
fan 3
15.9 ka
13.7 ka
14.0 ka
D NW
2,467 m
SE
fan 19 3 inch
fan 7 3 inch
fan 20 3 inch
19.6 ka
16.0 ka
17.7 ka
17.2 ka
clsvffmc
E
fan 15
fan 18
fan 23 3 inch
fan 16 3 inch
fan 8
fan 14 3 inch
fan 13 3 inch
fan 21 3 inch
fan 12 3 inch
fan 9
fan 1
fan 17
fan 10
fan 11
fan 24 3 inch
fan 5
fan 2
fan 19 3 inch
fan 4
fan 6
fan 3
fan 20 3 inch
fan 7
N
2000 m

Figure 10. Dip-oriented core cross-sections on the X intraslope submarine fan. (A) Seafloor amplitude map showing locations of parts B-D. (B) Northern dip-section, showing no systematic upslope or downslope bed-thickness trends. (C) Central dip-section, suggesting an apparent backstepping trend, with younger sand beds deposited closer to the X channel mouth. Note that the youngest sand deposition correlates with the dashed line in Fig. 7B. (D) Southern dip-section, showing downdip pinchout of sand beds from the X channel mouth. Poor core recovery suggests the presence of thick, amalgamated sand beds.

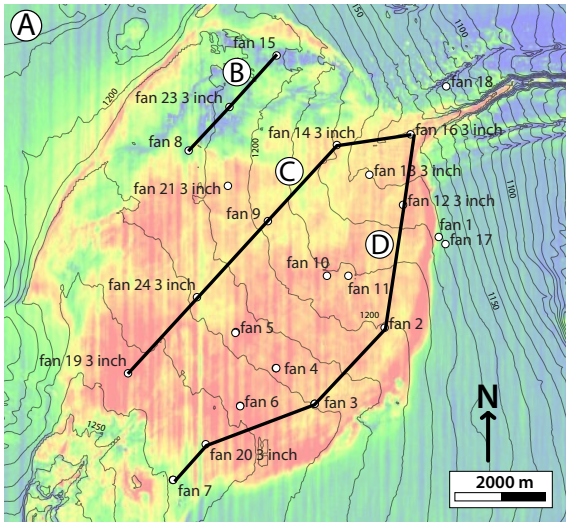
A
B
C
D
fan 15
fan 23 3 inch
fan 8
fan 14 3 inch
fan 16 3 inch
fan 18
fan 18 3 inch
fan 21 3 inch
fan 12 3 inch
fan 9
fan 1
fan 17
fan 10
fan 11
fan 24 3 inch
fan 5
fan 2
fan 19 3 inch
fan 4
fan 6
fan 3
fan 20 3 inch
fan 7
N
2000 m

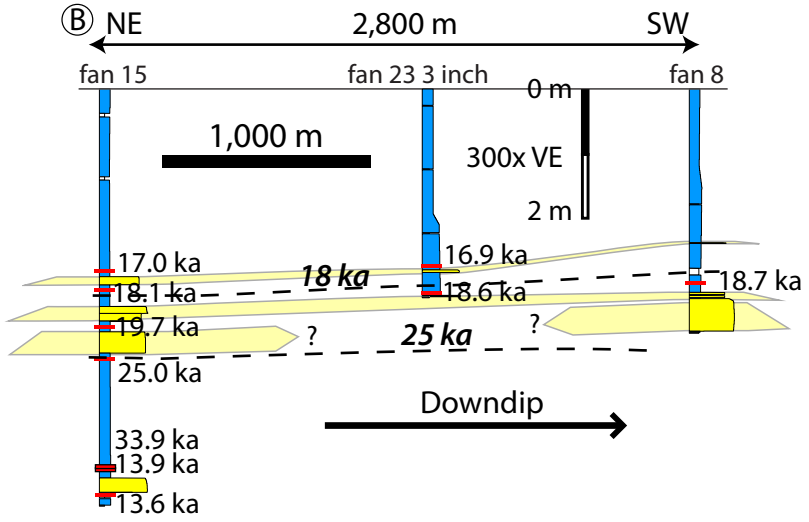
B
NE
2,800 m
SW
fan 15
fan 23 3 inch
fan 8
0 m
1,000 m
300x VE
2 m
17.0 ka
18.1 ka
19.7 ka
25.0 ka
33.9 ka
13.9 ka
13.6 ka
16.9 ka
18.6 ka
18.7 ka
18 ka
25 ka
?
Downdip

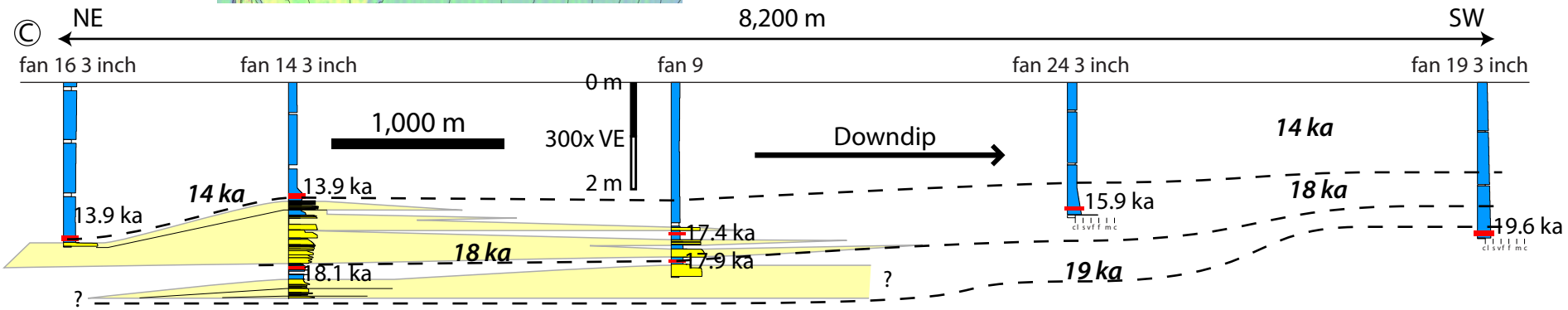
C
NE
8,200 m
SW
fan 16 3 inch
fan 14 3 inch
fan 9
fan 24 3 inch
fan 19 3 inch
0 m
1,000 m
300x VE
2 m
Downdip
14 ka
13.9 ka
13.9 ka
18 ka
18.1 ka
17.4 ka
17.9 ka
15.9 ka
19.6 ka
19 ka
?

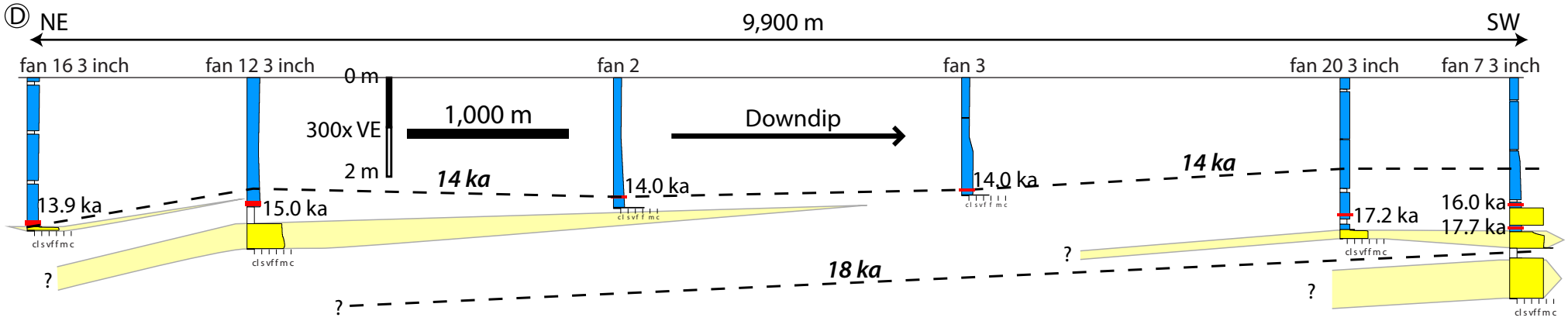
D
NE
9,900 m
SW
fan 16 3 inch
fan 12 3 inch
fan 2
fan 3
fan 20 3 inch
fan 7 3 inch
0 m
300x VE
2 m
1,000 m
Downdip
14 ka
13.9 ka
15.0 ka
14.0 ka
14.0 ka
17.2 ka
16.0 ka
17.7 ka
18 ka
?
cl sv ff mc

Figure 11. Conceptual diagram of the geomorphologic characteristics and facies distribution of an intraslope submarine fan (left) and base-of-slope submarine fan (right). Because of the bypass of muddy sediment and erosion at the distal edge of the basin, intraslope submarine lobe deposits may have more sand-rich facies architecture (left) than predicted by traditional lobe facies models (right). It is important to note, however, that intraslope fans can be more similar to the base-of-slope type if the intraslope basin is large compared to the flow size and/or flows are predominantly mud-rich.

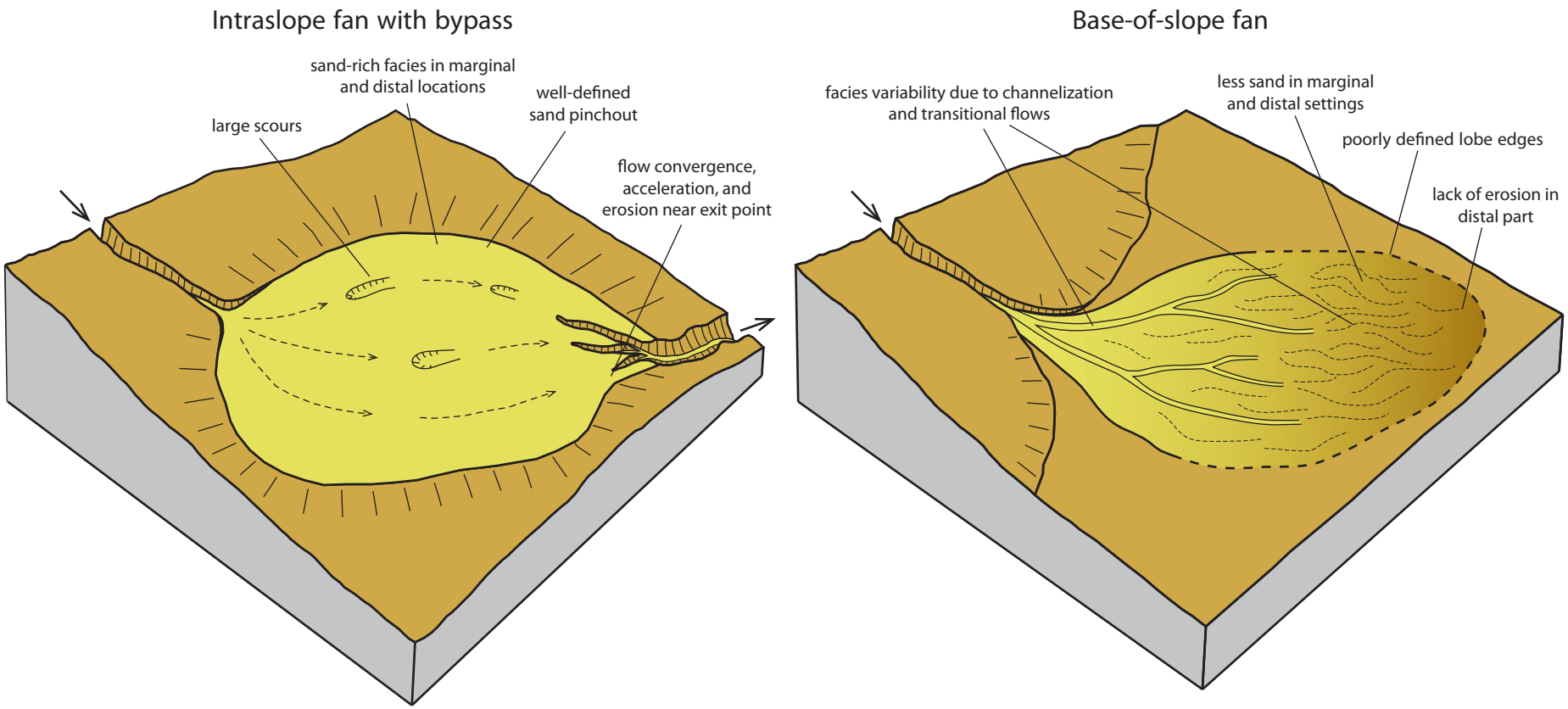
Intraslope fan with bypass
sand-rich facies in marginal and distal locations
well-defined sand pinchout
large scours
flow convergence, acceleration, and erosion near exit point
Base-of-slope fan
facies variability due to channelization and transitional flows
less sand in marginal and distal settings
poorly defined lobe edges
lack of erosion in distal part

500

501 Supplementary Figure 1. Cores from the X channel area, with photos, x-rays, visual descriptions,
502 grain size analyses, and radiocarbon ages.

503

BEND 1 (3 inch)

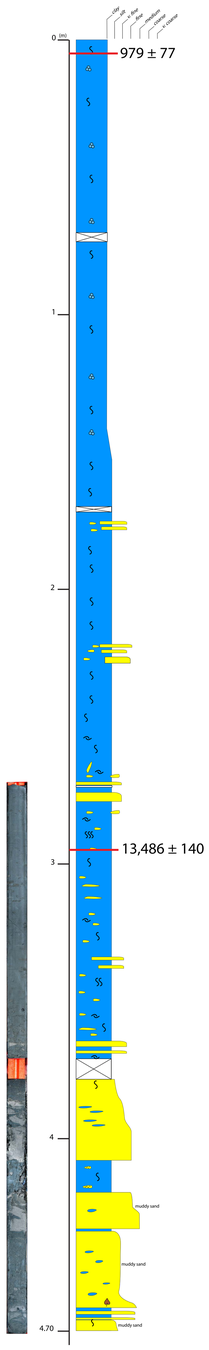

BEND 2 (3 inch)

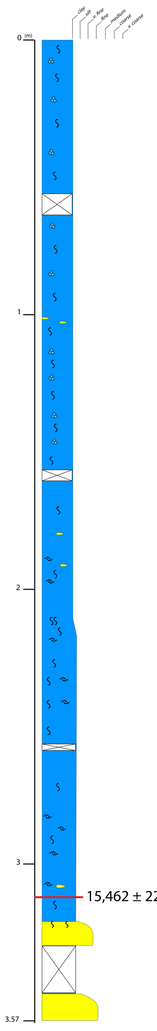

BEND 3

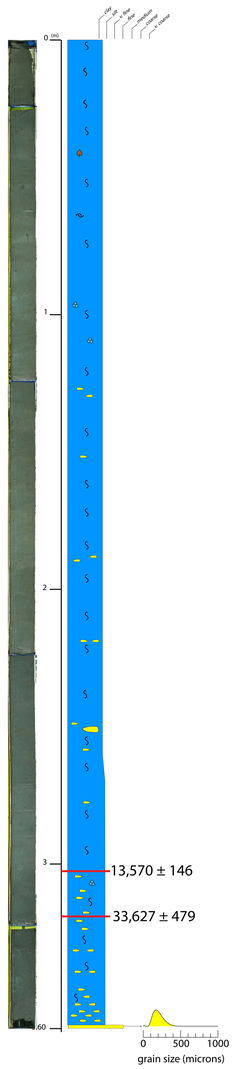

BEND 4

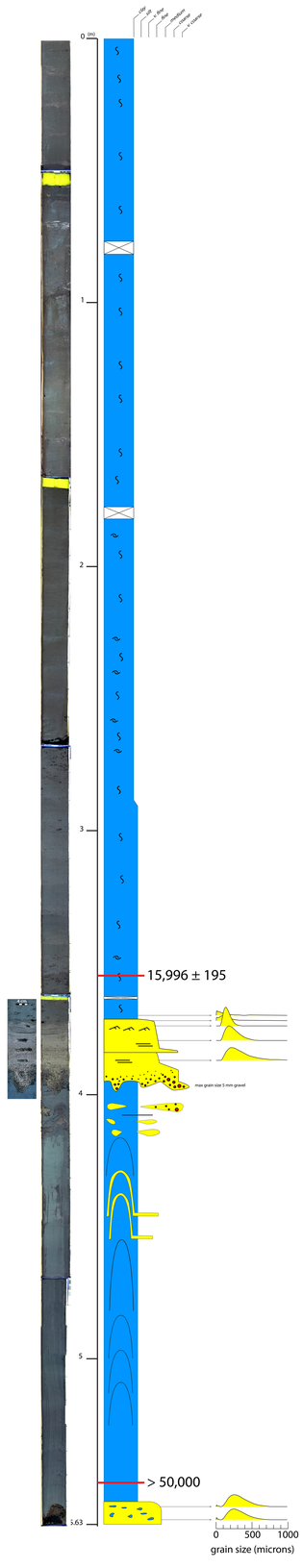

BEND 5

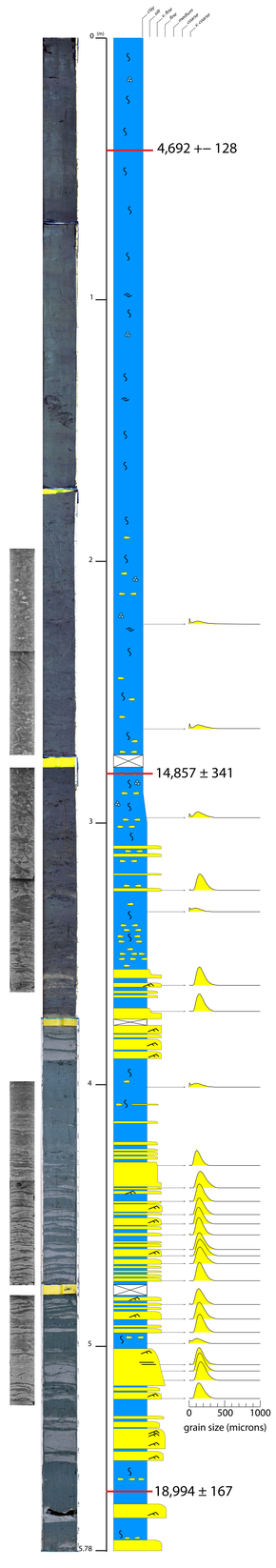

BEND 6

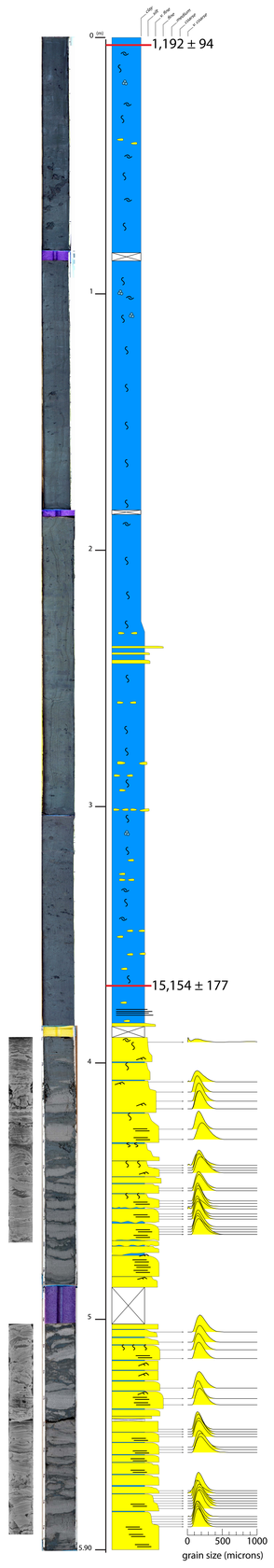

BEND 7 (3 inch)

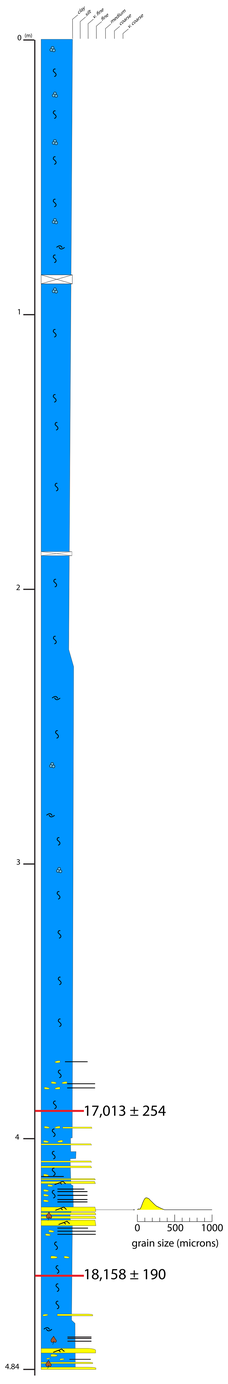

Legend for all core data

- mud
- sand
- no core recovery
- gravel
- bioturbation (muddy)
- bioturbation (sandy)
- organic matter
- plane / ripple lam.
- mud clast
- shell material
- slumping
- radiocarbon age — 20,076 ± 185

504

505 Supplementary Figure 2. Cores from the X intraslope submarine fan, with photos, x-rays, visual
506 descriptions, grain size analyses, and radiocarbon ages.

507

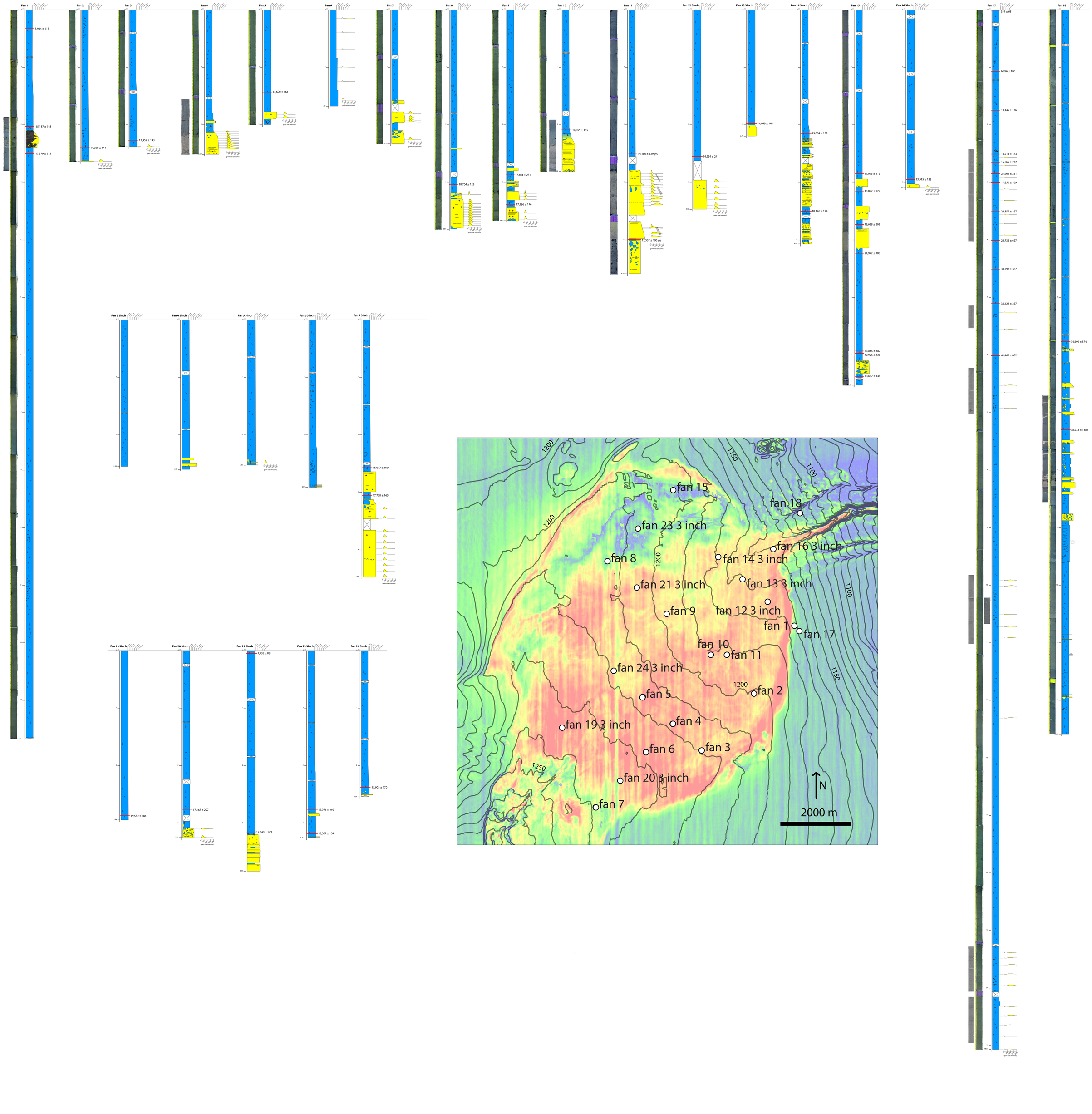
Fan 1
5,984 ± 115
15,187 ± 148
17,379 ± 215
Fan 2
14,029 ± 141
Fan 3
13,952 ± 143
Fan 4
Fan 5
13,690 ± 164
Fan 6
Fan 7
Fan 8
18,704 ± 129
Fan 9
17,404 ± 231
17,986 ± 176
Fan 10
14,055 ± 135
Fan 11
14,186 ± 629 yrs
17,567 ± 195 yrs
Fan 12 3inch
14,954 ± 241
Fan 13 3inch
14,049 ± 141
Fan 14 3inch
13,884 ± 139
18,176 ± 194
Fan 15
17,075 ± 216
18,097 ± 179
19,698 ± 209
24,972 ± 383
33,865 ± 387
13,926 ± 138
13,617 ± 144
Fan 16 3inch
13,915 ± 133
Fan 17
551 ± 68
6,926 ± 106
10,145 ± 136
13,213 ± 183
15,565 ± 232
21,965 ± 251
17,850 ± 169
22,359 ± 167
26,736 ± 627
30,792 ± 387
34,422 ± 367
41,460 ± 882
Fan 18
34,699 ± 574
38,273 ± 1382
grain size (microns)
Fan 3 3inch
Fan 4 3inch
Fan 5 3inch
Fan 6 3inch
Fan 7 3inch
16,017 ± 190
17,738 ± 165
Fan 19 3inch
19,552 ± 184
Fan 20 3inch
17,168 ± 227
Fan 21 3inch
1,438 ± 88
17,948 ± 179
Fan 23 3inch
16,974 ± 249
18,567 ± 154
Fan 24 3inch
15,903 ± 170
1200
1150
1100
1250
fan 15
fan 18
fan 23 3 inch
fan 16 3 inch
fan 8
fan 14 3 inch
fan 21 3 inch
fan 13 3 inch
fan 9
fan 12 3 inch
fan 1
fan 17
fan 10
fan 11
fan 24 3 inch
fan 5
fan 2
fan 4
fan 19 3 inch
fan 6
fan 3
fan 20 3 inch
fan 7
N
2000 m

508

509 Supplementary Table. Radiocarbon age data.

510

sample name (depth in cm)	CAMS #	$d^{13}C$	fraction of Modern	±	$D^{14}C$	±	^{14}C age (uncalibrated)	±	Calibrated age	(+) error	(-) error
bend 1_3in 0-10	162743	1	0.83660	0.00292	-163.39759	2.92100	1435	30	979	77	69
bend 1_3in 290-300	162744	1	0.22305	0.00096	-776.94832	0.96312	12050	35	13486	140	117
bend 2 3 inch 308-316	166394	1	0.18991	0.00100	-810.09466	0.99937	13345	45	15462	220	198
Bend 3 300-305	168266	1	0.22102	0.00108	-778.98077	1.08410	12125	40	13570	146	137
bend 3 315-323	166396	1	0.02442	0.00060	-975.58263	0.60196	29820	200	33627	364	479
bend 4 350-360	162745	1	0.17824	0.00098	-821.75755	0.97872	13855	45	16184	179	190
bend 4 350-360	162777	1	0.18154	0.00090	-818.46127	0.90494	13705	45	15996	185	195
bend 4 544-550	160746	0	0.00210	0.00051	-997.90240	0.51238	49500	2000	> 50000	-	-
bend 5 40-46	162746	1	0.57195	0.00231	-428.05137	2.31069	4490	35	4692	111	128
bend 5 274-280	162747	1	0.19911	0.00090	-800.89254	0.90477	12965	40	14898	239	274
bend 5 274-280	162776	1	0.19964	0.00094	-800.35610	0.93688	12945	40	14857	257	341
bend 5 553-558	162748	1	0.13377	0.00080	-866.22648	0.80181	16160	50	18994	167	126
bend 6 0-6	162718	1	0.81733	0.00294	-182.66848	2.94087	1620	30	1192	72	94
bend 6 367-373	162719	1	0.19529	0.00093	-804.70800	0.93110	13120	40	15154	149	177
bend 7 3in 387-393	163615	0	0.16629	0.00086	-833.71424	0.85831	14410	45	17013	197	254
bend 7 3in 447-453	163616	0	0.14807	0.00084	-851.93494	0.84139	15345	50	18158	173	190
fan 1 30-36	160747	0	0.49794	0.00175	-502.06045	1.75378	5600	30	5984	115	80
fan 1 200-206	163617	0	0.19458	0.00095	-805.42038	0.94705	13150	40	15187	143	148
fan 1 247-253	163618	0	0.16106	0.00091	-838.93863	0.90990	14670	50	17379	181	215
fan 10 206-212	166397	1	0.20916	0.00089	-790.83720	0.88951	12570	35	14055	119	135
fan 11 248-254	160777	0	0.20774	0.00353	-792.25993	3.53371	12620	140	14186	629	405
fan 11 400-410	160748	0	0.15806	0.00070	-841.94422	0.69968	14820	40	17567	195	178
fan 12_3in 250-260	162720	1	0.19831	0.00088	-801.68557	0.88424	12995	40	14954	192	241
fan 13 3 inch 206-216	166398	1	0.20920	0.00099	-790.79811	0.98588	12565	40	14049	126	141
fan 14 3in 210-220	163625	0	0.21351	0.00094	-786.48835	0.94038	12405	40	13884	139	131
fan 14 3in 347-353	163626	0	0.14773	0.00089	-852.27354	0.88658	15360	50	18176	170	194
fan 15 282-288	160749	0	0.16534	0.00072	-834.66001	0.71762	14455	35	17075	209	216
fan 15 312-318	160750	0	0.14901	0.00080	-850.98716	0.79685	15295	45	18097	179	170
fan 15 370-376	160751	0	0.12468	0.00065	-875.32050	0.65101	16725	45	19698	209	170
fan 15 420-426	160754	0	0.07219	0.00056	-927.81164	0.55595	21110	70	24972	278	383
fan 15 594-600	166399	1	0.21235	0.00099	-787.64809	0.98726	12445	40	13926	138	136
fan 15 589-597	168264	1	0.02351	0.00064	-976.48686	0.63694	30130	220	33865	387	375
Fan 15 634-640	168265	1	0.21979	0.00087	-780.20906	0.87175	12170	35	13617	144	141
fan 16_3in 290-300	162721	1	0.21269	0.00091	-787.31181	0.90719	12435	35	13915	133	129
fan 17 0-2	163627	0	0.88764	0.00312	-112.35553	3.12169	955	30	551	68	50
fan 17 450-452	163629	0	0.03495	0.00086	-965.05355	0.86355	26940	200	30792	300	387
fan 17 600-603	160757	0	0.00960	0.00053	-990.40422	0.52930	37320	450	41460	701	882
fan 17 250-252	163628	0	0.23215	0.00217	-767.85270	2.16948	11730	80	13213	172	183
fan 17 350-352	160755	0	0.09554	0.00059	-904.46337	0.59285	18865	50	22359	135	167
Fan 17 264-266	168262	1	0.18837	0.00083	-811.63482	0.83183	13410	40	15565	192	232
Fan 17 284-286	168263	1	0.09955	0.00067	-900.44994	0.67432	18530	60	21965	251	187
Fan 17_106-108	165166	0	0.44844	0.00162	-551.56063	1.62076	6440	30	6926	103	106
Fan 17_174-176	165167	0	0.31451	0.00116	-685.49060	1.15917	9290	30	10145	37	136
Fan 17_300-302	165168	0	0.15332	0.00069	-846.68216	0.69006	15065	40	17850	151	169
Fan 17_400-402	165169	0	0.05814	0.00201	-941.86298	2.00526	22850	280	26736	587	627
Fan 17_510-512	165170	0	0.02147	0.00047	-978.52730	0.47224	30850	180	34422	351	367
fan 18 574-580	163630	0	0.02061	0.00073	-979.38639	0.73032	31180	290	34699	572	574
fan 18 727-733	163631	0	0.01400	0.00074	-985.99738	0.73560	34290	430	38273	1032	1382
fan 18 970-976	-	-	-	-	-	-	-	-	> 50000	-	-
fan 19 3 inch 282-292	166395	1	0.12667	0.00068	-873.33180	0.67758	16600	45	19552	184	176
fan 20 3in 274-280	163632	0	0.16420	0.00085	-835.79891	0.85085	14515	45	17168	227	194
fan 21_3in 0-10	163681	0	0.79032	0.00275	-209.67888	2.74990	1890	30	1438	82	88
fan 21_3in 310-320	162722	1	0.15161	0.00090	-848.38726	0.90394	15155	50	17948	171	179
fan 23 3in 274-280	163633	0	0.16686	0.00085	-833.13720	0.84671	14385	45	16974	203	249
fan 23 3in 315-321	163634	0	0.14172	0.00085	-858.28439	0.84655	15695	50	18567	143	154
Fan 24 3 inch 234-242	166393	1	0.18321	0.00088	-816.78927	0.87701	13635	40	15903	170	168
fan 2 237-243	163619	0	0.20981	0.00100	-790.18968	1.00180	12545	40	14029	127	141
fan 3 224-230	163620	0	0.20474	0.00104	-795.26290	1.04098	12740	45	13952	142	143
fan 5 140-146	163621	0	0.21823	0.00101	-781.76569	1.00678	12230	40	13690	140	164
fan 7 3 inch 302-308	166400	1	0.15534	0.00073	-844.66102	0.73459	14960	40	17738	165	165
fan 7 3 inch 254-260	168267	1	0.18119	0.00083	-818.80843	0.82831	13720	40	16017	177	190
fan 8 301-307	163622	0	0.13922	0.00085	-860.77593	0.84622	15840	50	18704	111	129
fan 9 335-341	163624	0	0.15090	0.00087	-849.09775	0.87195	15190	50	17986	176	165
fan 9 284-290	163623	0	0.16055	0.00106	-839.45139	1.05543	14690	60	17404	195	231

REFERENCES

Abd El-Gawad, S.M., Pirmez, C., Cantelli, A., Minisini, D., Sylvester, Z., and Imran, J., 2012a, 3-D numerical simulation of turbidity currents in submarine canyons off the Niger Delta: Marine Geology, v. 326-328, p. 55–66, doi: 10.1016/j.margeo.2012.06.003.

Abd El-Gawad, S., Cantelli, A., Pirmez, C., Minisini, D., Sylvester, Z., and Imran, J., 2012b, Three-dimensional numerical simulation of turbidity currents in a submarine channel on the seafloor of the Niger Delta slope: Journal of Geophysical Research, v. 117, p. C05026, doi: 10.1029/2011JC007538.

Adeogba, A.A., McHargue, T.R., and Graham, S.A., 2005, Transient fan architecture and depositional controls from near-surface 3-D seismic data, Niger Delta continental slope: AAPG Bulletin, v. 89, p. 627–643, doi: 10.1306/11200404025.

Allen, J., 1965, Late Quaternary Niger delta, and adjacent areas: sedimentary environments and lithofacies: AAPG Bulletin, v. 49, p. 547–600.

Allen, J., 1964, The Nigerian continental margin: bottom sediments, submarine morphology and geological evolution: Marine Geology, v. 1, p. 289–332, doi: 10.1016/0025-3227(64)90018-0.

Babonneau, N., Savoye, B., Cremer, M., and Bez, M., 2010, Sedimentary Architecture in Meanders of a Submarine Channel: Detailed Study of the Present Congo Turbidite Channel (Zaiango Project): Journal of Sedimentary Research, v. 80, p. 852–866, doi: 10.2110/jsr.2010.078.

Bouma, A.H., 1962, Sedimentology of Some Flysch Deposits: A Graphic Approach to Facies Interpretation: Amsterdam, Elsevier, 168 p.

Cantelli, A., Pirmez, C., Johnson, S., and Parker, G., 2011, Morphodynamic and Stratigraphic Evolution of Self-Channelized Subaqueous Fans Emplaced by Turbidity Currents: Journal of Sedimentary Research, v. 81, p. 233–247, doi: 10.2110/jsr.2011.20.

Covault, J.A., and Romans, B.W., 2009, Growth patterns of deep-sea fans revisited: Turbidite-system morphology in confined basins, examples from the California Borderland: Marine Geology, v. 265, p. 51–66, doi: 10.1016/j.margeo.2009.06.016.

Covault, J.A., Romans, B.W., FILDANI, A., McGann, M., and Graham, S.A., 2010, Rapid Climatic Signal Propagation from Source to Sink in a Southern California Sediment ‐ Routing System: The Journal of Geology, v. 118, p. 247‐259, doi: 10.1086/651539.

Covault, J. A. (2011) Submarine Fans and Canyon-Channel Systems: A Review of Processes, Products, and Models. Nature Education Knowledge 3(10):4; http://www.nature.com/scitable/knowledge/library/submarine-fans-and-canyon-channel-systems-a-24178428

Covault, J.A., Kostic, S., Paull, C.K., Ryan, H.F., and Fildani, A., 2014, Submarine channel initiation, filling and maintenance from sea-floor geomorphology and morphodynamic modelling of cyclic steps: Sedimentology, v. 61, p. 1031–1054, doi: 10.1111/sed.12084.

Damuth, J.E., 1994, Neogene gravity tectonics and depositional processes on the deep Niger Delta continental margin: Marine and Petroleum Geology, v. 11, p. 320–346, doi: 10.1016/0264-8172(94)90053-1.

Deptuck, M.E., Piper, D.J.W., Savoye, B., and Gervais, A., 2008, Dimensions and architecture of late Pleistocene submarine lobes off the northern margin of East Corsica: Sedimentology, v. 55, p. 869–898, doi: 10.1111/j.1365-3091.2007.00926.x.

Deschamps, P., Durand, N., Bard, E., Hamelin, B., Camoin, G., Thomas, A.L., Henderson, G.M., Okuno, J., and Yokoyama, Y., 2012, Ice-sheet collapse and sea-level rise at the Bølling warming 14,600 years ago: Nature, v. 483, p. 559–564, doi: 10.1038/nature10902.

Doust, H., and Omatsola, E., 1989, Niger delta: *in* Edwards, J.D., and Santogrossi, P.A., eds., Divergent/Passive Margin Basins: American Association of Petroleum Geologists Memoir, v. 48, p. 201-238.

Evamy, B.D., Haremboure, J., and Kamerling, P., 1978, Hydrocarbon habitat of Tertiary Niger delta: AAPG Bulletin, v. 62, p. 1–39.

Fernandez, R.L., Cantelli, A., Pirmez, C., Sequeiros, O., and Parker, G., 2014, Growth Patterns of Subaqueous Depositional Channel Lobe Systems Developed Over A Basement With A Downdip Break In Slope: Laboratory Experiments: Journal of Sedimentary Research, v. 84, p. 168–182, doi: 10.2110/jsr.2014.10.

Flint, S.S., Hodgson, D.M., Sprague, A.R., Brunt, R.L., van der Merwe, W.C., Figueiredo, J., Prelat, A., Box, D., Di Celma, C., and Kavanagh, J.P., 2011, Depositional architecture and sequence stratigraphy of the Karoo basin floor to shelf edge succession, Laingsburg depocentre, South Africa: Marine and Petroleum Geology, v. 28, p. 658–674, doi: 10.1016/j.marpetgeo.2010.06.008.

Flood, R. D., Pirmez, C., and Yin, H. 1997, The compressional-wave velocity of Amazon Fan sediments: Calculation from petrophysical properties and variation with clay content, in Flood, R. D., Piper, D. J. W., Klaus, A., and Peterson, L. C., Proceedings of the Ocean Drilling Project, Scientific Results 155, p. 477–496.

Hansen, L. A., Callow, R. H., Kane, I. A., Gamberi, F., Rovere, M., Cronin, B. T., & Kneller, B. C., 2015, Genesis and character of thin-bedded turbidites associated with submarine channels. Marine and Petroleum Geology, v. 67, p. 852-879, doi: 10.1016/j.marpetgeo.2015.06.007.

Jegou, I., Savoye, B., Pirmez, C., and Droz, L., 2008, Channel-mouth lobe complex of the recent Amazon Fan: The missing piece: Marine Geology, v. 252, p. 62–77, doi: 10.1016/j.margeo.2008.03.004.

Jobe, Z.R., Sylvester, Z., Parker, A.O., Howes, N., Slowey, N., and Pirmez, C., 2015, Rapid Adjustment of Submarine Channel Architecture To Changes In Sediment Supply: Journal of Sedimentary Research, v. 85, p. 729–753, doi: 10.2110/jsr.2015.30.

Kane, I. A., McCaffrey, W. D., and Martinsen, O. J., 2009, Allogenic vs. autogenic controls on megaflute formation. Journal of Sedimentary Research, v. 79, p. 643-651, doi: 10.2110/jsr.2009.072.

Lisiecki, L.E., and Raymo, M.E., 2005, A Pliocene-Pleistocene stack of 57 globally distributed benthic $\delta^{18}O$ records: Paleoceanography, v. 20.1., PA1003, doi:10.1029/2004PA001071

Lowe, D.R., 1982, Sediment gravity flows: II Depositional models with special reference to the deposits of high-density turbidity currents: Journal of Sedimentary Research, v. 52, p. 279–297.

Luthi, S., 1981, Experiments on non-channelized turbidity currents and their deposits: Marine Geology, v. 40, p. M59–M68.

Lyons, W.J.I., 2004, Quantifying Channelized Submarine Depositional Systems From Bed to Basin Scale: Massachusetts Institue of Technology-Woods Hole Oceanographic Institution, Ph.D. thesis, 252 p.

Maier, K.L., Fildani, A., Paull, C.K., McHargue, T.R., Graham, S.A., and Caress, D.W., 2013, Deep-sea channel evolution and stratigraphic architecture from inception to abandonment from high-resolution Autonomous Underwater Vehicle surveys offshore central California: Sedimentology, v. 60, p. 935–960, doi: 10.1111/j.1365-3091.2012.01371.x.

590 Mulder, T., and Syvitski, J., 1995, Turbidity currents generated at river mouths during exceptional discharges to the
591 world oceans: The Journal of Geology, v. 103, p. 285–299.

592 Mutti, E., & Ricci Lucchi, F., 1972, Le torbiditi dell'Appennino settentrionale: introduzione all'analisi di facies.
593 Memorie della Societa Geologica Italiana, v. 11(2), p. 161-199.

594 Mutti, E., and Normark, W.R., 1987, Comparing examples of modern and ancient turbidite systems: problems and
595 concepts, *in* Leggett, J.K. and Zuffa, G.G. eds., Marine Clastic Sedimentology, p. 1–38.

596 Normark, W.R., 1970, Channel piracy on Monterey deep-sea fan: Deep Sea Research, v. 17, p. 837–846, doi:
597 10.1016/0011-7471(70)90001-X.

598 Parker, A.O., Schmidt, M.W., Jobe, Z.R., and Slowey, Niall, 2016, A New Perspective on West African
599 Hydroclimate During the Last Deglaciation: Earth and Planetary Science Letters, v. 449, p. 79-88,
600 doi:10.1016/j.epsl.2016.05.038.

601 Parsons, J.D., Schweller, W.J., and Stelting, C.W., 2002, A preliminary experimental study of turbidite fan deposits:
602 Journal of Sedimentary Research, v. 72, p. 619–628.

603 Piper, D., and Normark, W.R., 2001, Sandy fans--from Amazon to Hueneme and beyond: AAPG Bulletin, v. 85, p.
604 1407–1438.

605 Pirmez, C., Beaubouef, R.T., Friedmann, S.J., And Mohrig, D.C., 2000, Equilibrium Profile and Base Level in
606 Submarine Channels: Examples from Late Pleistocene Systems and Implications for the Architecture of
607 Deepwater Reservoirs: *in* P. Weimer, R. M. Slatt, J. Coleman, N. C. Rosen, H. Nelson, A. H. Bouma, M. J.
608 Styzen, & D. T. Lawrence (Eds.), Deep-water reservoirs of the world: Gulf Coast Societies Foundation
609 20th Annual Research Conference, p. 782-805.

610 Pirmez, C., Prather, B.E., Mallarino, G., O'Hayer, W.W., Droxler, A.W., and Winker, C.D., 2012,
611 Chronostratigraphy of the Brazos–Trinity depositional System, Western Gulf of Mexico: implications for
612 deepwater depositional models, *in* Prather, B.E., Deptuck, M.E., Mohrig, D., van Hoorn, B., and Wynn, R.,
613 eds., Application of the Principles of Seismic Geomorphology to Continental-Slope and Base-of-Slope
614 Systems: Case Studies from Seafloor and Near-Seafloor Analogues: SEPM, Special Publication 99, SEPM
615 (Society for Sedimentary Geology), p. 111-143.

616 Prather, B.E., Booth, J.R., Steffens, G.S., and Craig, P.A., 1998, Classification, lithologic calibration, and
617 stratigraphic succession of seismic facies of intraslope basins, deep-water Gulf of Mexico: AAPG Bulletin,
618 v. 82, p. 701–728.

619 Prather, B.E., Pirmez, C., Sylvester, Z., And Prather, D.S., 2012a, Stratigraphic Response to Evolving
620 Geomorphology in a Submarine Apron Perched on the Upper Niger Delta Slope, *in* Prather, B.E., Deptuck,
621 M.E., Mohrig, D.C., van Hoorn, B., and Wynn, R.B., eds., Application of the Principles of Seismic
622 Geomorphology to Continental-Slope and Base-of-Slope Systems: Case Studies from Seafloor and Near-
623 Seafloor Analogues: SEPM Special Publication 99, SEPM (Society for Sedimentary Geology), p. 145-161.

624 Prather, B.E., Pirmez, C., Winker, C.D., 2012b, Stratigraphy of Linked Intraslope Basins: Brazos–Trinity System
625 Western Gulf of Mexico, *in* Prather, B.E., Deptuck, M.E., Mohrig, D.C., van Hoorn, B., and Wynn, R.B.,
626 eds., Application of the Principles of Seismic Geomorphology to Continental-Slope and Base-of-Slope
627 Systems: Case Studies from Seafloor and Near-Seafloor Analogues: SEPM Special Publication 99, SEPM
628 (Society for Sedimentary Geology), p. 83-109.

629 Prélat, A., Hodgson, D.M., and Flint, S.S., 2009, Evolution, architecture and hierarchy of distributary deep-water
630 deposits: a high-resolution outcrop investigation from the Permian Karoo Basin, South Africa:
631 Sedimentology, v. 56, p. 2132–2154, doi: 10.1111/j.1365-3091.2009.01073.x.

Prélat, A., Covault, J.A., Hodgson, D.M., Fildani, A., and Flint, S.S., 2010, Intrinsic controls on the range of volumes, morphologies, and dimensions of submarine lobes: Sedimentary Geology, v. 232, p. 66–76, doi: 10.1016/j.sedgeo.2010.09.010.

Pyrcz, M.J., Catuneanu, O., and Deutsch, C.V., 2005, Stochastic surface-based modeling of turbidite lobes: AAPG Bulletin, v. 89, p. 177–191, doi: 10.1306/09220403112.

Reimer, P.J., Baillie, M., Bard, E., et al., 2009, IntCal09 and Marine09 radiocarbon age calibration curves, 0-50,000 years cal BP: Radiocarbon, v. 51, p. 1111–1150, doi: 10.3916/C34-2010-02-03.

Romans, B.W., Normark, W.R., McGann, M.M., Covault, J.A., and Graham, S.A., 2009, Coarse-grained sediment delivery and distribution in the Holocene Santa Monica Basin, California: Implications for evaluating source-to-sink flux at millennial time scales: Geological Society of America Bulletin, v. 121, p. 1394–1408, doi: 10.1130/B26393.1.

Romans, B.W., Castelltort, S., Covault, J.A., Fildani, A., and Walsh, J.P., 2016, Environmental signal propagation in sedimentary systems across timescales: Earth Science Reviews, v. 153, p. 7–29, doi: 10.1016/j.earscirev.2015.07.012.

Sheets, B.A., Hickson, T.A., and Paola, C., 2002, Assembling the stratigraphic record: Depositional patterns and time-scales in an experimental alluvial basin: Basin Research, v. 14, p. 287–301.

Smith, R. D. A., 1987, The Griestoniensis Zone Turbidite System, Welsh Basin. *in* Leggett, J. and Zuffa, G., eds., Marine Clastic Sedimentology (pp. 89-107), Springer Netherlands.

Smith, R.D.A. 2004, Silled Sub-Basins to Connected Tortuous Corridors: Sediment Distribution Systems on Topographically Complex Sub-Aqueous Slopes. *in* Lomas, S. A. & Joseph, P., eds., Confined Turbidite Systems. Geological Society, London, Special Publications, 222, p. 23-43.

Straub, K.M., Paola, C., Mohrig, D., Wolinsky, M.A., and George, T., 2009, Compensational Stacking of Channelized Sedimentary Deposits: Journal of Sedimentary Research, v. 79, p. 673–688, doi: 10.2110/jsr.2009.070.

Stuiver, M. and Reimer, P.J., and Reimer, R.W., 2005, CALIB 5.0, http://calib.qub.ac.uk/calib/ site accessed 4/1/16

Sylvester, Z., Deptuck, M., Prather, B., Pirmez, C., and O'Byrne, C., 2012, Seismic stratigraphy of a shelf-edge delta and linked submarine channels in the north-eastern gulf of Mexico, *in* Prather, B.E., Deptuck, M.E., Mohrig, D.C., van Hoorn, B., and Wynn, R.B., eds., Application of the Principles of Seismic Geomorphology to Continental-Slope and Base-of-Slope Systems: Case Studies from Seafloor and Near-Seafloor Analogues: SEPM Special Publication 99, SEPM (Society for Sedimentary Geology), p. 31-59.

Sylvester, Z., Cantelli, A., and Pirmez, C., 2015, Stratigraphic evolution of intraslope minibasins: Insights from surface-based model: AAPG Bulletin, v. 99, p. 1099–1129, doi: 10.1306/01081514082.

Vittori, J., Morash, A., Savoye, B., Marsset, T., Lopez, M., Droz, L., & Cremer, M., 2000, The Quaternary Congo deep-sea fan: preliminary results on reservoir complexity in turbiditic systems using 2D high resolution seismic and multibeam data. *in* P. Weimer, R. M. Slatt, J. Coleman, N. C. Rosen, H. Nelson, A. H. Bouma, M. J. Styzen, & D. T. Lawrence (Eds.), Deep-water reservoirs of the world: Gulf Coast Societies Foundation 20th Annual Research Conference, p. 1045–1058.

Walker, R.G., 1978, Deep-water sandstone facies and ancient submarine fans: models for exploration for stratigraphic traps: AAPG Bulletin, v. 62, p. 932–966.